A hybrid integro-differential model for the early development of the zebrafish posterior lateral line

Highlights

A hybrid integro-differential model for the early development of the zebrafish posterior lateral line

Annachiara Colombi, Marco Scianna, Luigi Preziosi

- A mathematical model for the early development of zebrafish PLL is proposed.
- We propose an integro-differential mathematical model based on a hybrid approach.
- A microscopic/discrete particle-based description is used for cell dynamics.
- A continuous description is used for the distribution of chemicals (SDF1a and FGF10).
- Boolean variables are used for molecular receptors (*Cxcr4*/*Cxcr7* and *fgfr1*).
- Cell phenotypic transitions and proliferation are included as well.
- Our results capture the normal evolution of embryos and experimental manipulations.
- All the included features are fundamental for the correct development of the embryo.

A hybrid integro-differential model for the early development of the zebrafish posterior lateral line

Annachiara Colombi[a,*], Marco Scianna[b], Luigi Preziosi[b]

[a] *Istituto Nazionale di Alta Matematica "F. Severi" - INdAM Reseach Unit at Politecnico di Torino, Corso Duca degli Abruzzi 24, 10129, Torino, Italy*
[b] *Department of Mathematical Sciences "G. L. Lagrange", Politecnico di Torino, Corso Duca degli Abruzzi 24, 10129, Torino, Italy*

Abstract

The aim of this work is to provide a mathematical model to describe the early stages of the embryonic development of zebrafish *posterior lateral line* (PLL). In particular, we focus on evolution of PLL proto-organ (said *primordium*), from its formation to the beginning of the cyclical behavior that amounts in the assembly of immature proto-neuromasts towards its caudal edge accompanied by the deposition of mature proto-neuromasts at its rostral region. Our approach has an hybrid integro-differential nature, since it integrates a microscopic/discrete particle-based description for cell dynamics and a continuous description for the evolution of the spatial distribution of chemical substances (i.e., the stromal-derived factor SDF1a and the fibroblast growth factor FGF10). Boolean variables instead implement the expression of molecular receptors (i.e., *Cxcr4*/*Cxcr7* and *fgfr1*). Cell phenotypic transitions and proliferation are included as well. The resulting numerical simulations show that the model is able to qualitatively and quantitatively capture the evolution of the *wild-type* (i.e., normal) embryos as well as the effect of known experimental manipulations. In particular, it is shown that cell proliferation, intercellular adhesion, FGF10-driven dynamics, and a polarized expression of SDF1a receptors are all fundamental for the correct development of the zebrafish posterior lateral line.

Keywords: coordinated cell migration, proto-neuromasts formation and deposition, cell phenotypic differentiation, non-local interactions, non-local chemotaxis
2020 MSC: 34K34, 37N25, 45J05, 92C17

1. Introduction

The *lateral line* is a sensory organ that is present in both fishes and amphibians, and has the function to detect water displacements [28]. It is therefore involved in several fundamental activities for animal life such as prey and

*Corresponding author: annachiara.colombi@polito.it

predator detection, obstacle avoidance, collective swimming and courtship [15]. In general, the lateral line consists of (i) a set of mechanosensory elements, named *neuromasts*, arranged in a species-specific pattern over the surface of animal's body, and (ii) a network of afferent neurons that carry information from the brain to the neuromasts and *viceversa* [15]. The *posterior lateral line* (PLL) is the portion of the lateral line located over the trunk and tail; the rest of the organ, comprising the neuromasts over the head of the animal, is instead referred to as *anterior lateral line* [15].

The development of PLL in zebrafish (*Danio rerio*) embryos is a benchmark process widely analyzed by biologists to study coordinated cell organization and collective migration [14, 19, 24, 30]. It is indeed a good predictive model to shed lights both on physiological organogenesis and on selected disorders in growth/repair mechanisms in humans, as nearly 70% of our genes are found also in zebrafish.

In particular, the development of zebrafish PLL begins around 19 hours post egg fertilization (hpf) with the formation of a small placode of about 100 epithelial cells, named *primordium* (PLLp), located within the horizontal myoseptum of the animal, just caudal to the otic vesicle, as shown in the top left panel of Fig. 1 [20, 28]. The entire PLL system then assembles in two phases [15, 23]. Over the following 24-28 hours, the primordium migrates towards the tail of the animal depositing six-to-eight neuromast progenitors, termed *proto-neuromasts* (or *rosettes*, due to their characteristic shape), which result distributed along the flanks of the embryo, as sketched by the red dots in the bottom left panel of Fig. 1. Trails of interneuromastic cells are possibly located between consecutive rosettes. Successively, during post-embryonic growth, cells within the proto-neuromasts differentiate into hair and supporting individuals, giving rise to fully developed neuromasts. To complete the PLL system, additional mechanosensory organs are provided by the proliferation of interneuromastic cells and by the development of additional primordia, while a proper neuronal network forms connecting them to the brain.

We here propose a hybrid multiscale model able to reproduce and analyze selected aspects of the previously-described first phases of zebrafish PLL development, i.e., from primordium formation to the deposition of the first mature proto-neuromast and assembly of the fifth one (which in wild-type embryos occurs around 30 hpf, according to empirical evidences in [24], see the central left panel of Fig. 1). In particular, within our theoretical framework, cells are described as microscopic/discrete pointwise particles whereas diffusive chemicals and relative receptors are represented with a continuous approach, i.e., through concentrations or Boolean binary variables. The overall system evolution is therefore determined by the coupling between a set of ordinary differential equations (ODEs) for cell dynamics and reaction-diffusion (RD) laws for molecular kinetics. Proper rules for cell phenotypic transitions and mitotic processes are introduced as well.

The contents presented in the rest of the paper are organized as follows. Section 2 is devoted to a detailed description of the main mechanisms regulating the early development of PLL. A review of the pertinent theoretical literature is

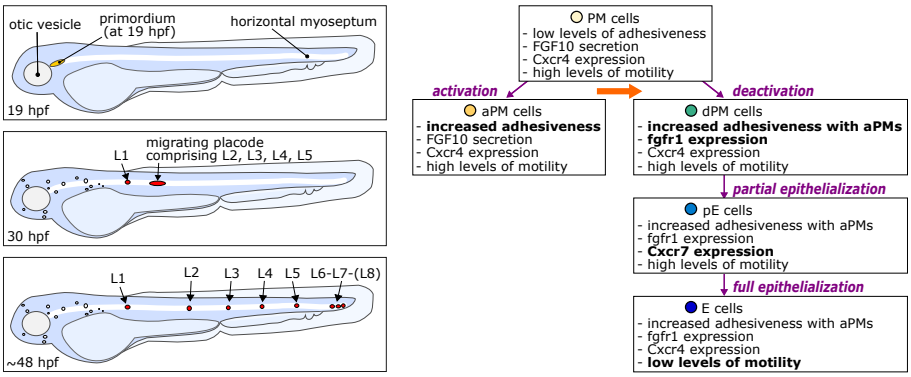

Figure 1: Top left panel: Initial position (i.e., at 19 hpf) of the progenitor primordium within the zebrafish embryonic body. It is located just behind the otic vesicle at the rostral extremum of the horizontal myoseptum. Central left panel: Characteristic primordium configuration at the assembly of the fifth rosette (L5) occurring around 30 hpf according to empirical evidence in [24]). Bottom left panel: Characteristic pattern of the deposited proto-neuromasts (labeled by L1-L8) at the end of zebrafish embryogenesis, i.e., about $24 - 28$ hpf. Right panel: Cell phenotypes with relative molecular state and possible transitions. The primordium is initially constituted by *pseudo-mesenchymal* ("PM") cells. Each PM individual can undergo two distinct fates. It can either activate, becoming an *activated pseudo-mesenchymal* ("aPM") cell, i.e., PM→aPM, or be deactivated by a surrounding individual, thereby becoming a *deactivated pseudo-mesenchymal* ("dPM"), i.e., PM→dPM. In this second case, it is then subjected by a multi-step epithelialization, it first assume a *partially epithelial* state ("pE") and then a *fully epithelial* ("E") phenotype, i.e., dPM→pE→E. A detailed description of cell types and phenotypic transitions is provided in Assumption (A2) in Section 2.

provided in Section 3. The hybrid mathematical model, based on the assumptions in Section 2, is introduced in Section 4. In Section 5, different numerical simulations will be reported. In particular, we will first deal with the reproduction of the normal PLL development, i.e., as observed in *wild-type* embryos. Then, selected manipulations of the system will be investigated highlighting the consistency between our numerical results and empirical evidences (when available). Some considerations on possible developments of the work will be discussed in Section 6. Finally, in Appendix A, we will give details on the estimate of the model parameters, both by clarifying which values have been taken from the literature and by justifying the choice of the others.

2. Biological background

We here summarize the main mechanisms underlying the early development of the zebrafish PLL, as observed both in *in vivo* and in *in vitro* experiments: they will constitute the simplified assumptions at the basis of the proposed mathematical model.

(A1) **Initial configuration.** The posterior lateral line primordium (PLLp) originates around 19 hpf as a homotypic placode composed of about 100

epithelial cells with mesenchymal characteristics (as specified in assumption (A2) below). They have an almost round morphology with a mean diameter of nearly 7 μm [20, 28]. The primordium is initially placed just behind the otic vesicle, at the rostral edge of the horizontal myoseptum, and presents an elliptical shape, i.e., elongated in the head-to-tail direction of the embryo (see Fig. 1, top left panel). In particular, as captured by experimental images in [17], the main axis of the placode at the onset of migration is 20-25 cell-long, whereas the secondary axis is 4-5 cell-wide.

(A2) **Cell types and phenotypic transitions.** The default/initial state of the cells forming the primordium is *pseudo-mesenchymal* ("PM") [22]. Regardless of their epithelial genotype, they in fact display an increased number of dynamic filopodia (resulting in high levels of motility) and a reduced expression of membrane junction proteins (resulting in low levels of adhesiveness). Moreover, PM cells produce chemical fibroblast growth factor 10 (FGF10) [24], while expressing the migratory-related receptor of the stromal-derived factor 1a (SDF1a), named *Cxcr4* [9].

These progenitor PM individuals may either maintain their state for the entire period of observation or undergo two distinct fates. Few of them singularly (i.e., at different time instants) activate and become the center of rosette-like structures that progressively form and mature (see assumptions (A4) and (A5) below). Such cells, hereafter denoted as *activated pseudo-mesenchymal* ("aPM"), are observed to maintain high levels of motility, the basal FGF10 secretion rate and the expression of SDF1a receptor *Cxcr4*, while increasing their adhesive ability.

Each aPM then induces a phenotypic transition, i.e., a sort of deactivation, of a cluster of PM cells in its surrounding, which will form the body of a rosette. These *deactivated pseudo-mesenchymal* individuals (hereafter identified by "dPM") are no longer able to produce FGF10, rather they start to express its receptor *fgfr1*.

dPM cells are further characterized by two sequential state changes. First, they undergo a *partial epithelialization* (and are labeled by "pE"), which involves the expression of the SDF1a non migratory-related receptor *Cxcr7*. Then, a complete epithelialization occurs (leading to *fully epithelial* cells, hereafter identified by the acronym "E"), which amounts in a dramatic drop of the individual migratory ability. Experimental studies further show that strong contact interactions between the over-adhesive aPM cells and the surrounding dPM, pE, and E agents are responsible for rosette stabilization [22, 24].

It is finally useful to remark that all the proposed phenotypic transitions, summarized in the scheme in Fig. 1 (right panel), do not involve significant morphological variations.

(A3) **Molecular substance and receptors.** The embryonic development of the zebrafish PLL is mainly regulated by the activity of two diffusive chemicals.

The fibroblast growth factor 10 (FGF10) is a placode endogenous substance constantly produced by PM and aPM cells (refer again to Fig. 1, right panel): it provides short-range signals within the primordium body, in particular towards *fgfr1* expressing cells (i.e., dPM, pE, and E individuals, see [8, 22]).

The stromal-derived factor 1a (SDF1a) is instead produced from about 20 hpf by a narrow stripe (i.e., nearly 3 cell-wide, see [15]) of the myoseptum substrate [10]. SDF1a represents an exogenous chemotactic cue for *Cxcr4* expressing individuals (i.e., PM, aPM, and dPM agents, see [9, 31]). In this respect, the non migratory-related receptor *Cxcr7* has an antagonistic effect against *Cxcr4*, since it temporarily masks a larger amount of the exogenous substance due to its ten-times higher affinity, as quantified in [9]. *Cxcr7*-expressing cells therefore affect the directional locomotion of the surrounding *Cxcr4*-expressing individuals by locally modifying the pattern of available SDF1a, see [9, 12, 16].

(A4) **Primordium segmentation and patterning.** As shown in [24], right after primordium formation, a first rosette (named L1) appears at anterior/rostral edge of the PLL primordium. Over the next hours, additional proto-neuromasts sequentially form just caudally one to each other. Once two to three rosettes have formed, as we will see in (A6), the placoid cluster begins to migrate along the stripe of SDF1a. The formation of a fourth caudal rosette (said L4) then correlates with the deposition of the firstly formed proto-neuromast (i.e., L1), which slows down and detaches from the trailing edge of the primordium. The subsequent assembly of the fifth rosette eventually gives rise to the cyclical behavior characteristic of the placode cluster, which amounts in the formation of a new proto-neuromast towards the caudal edge accompanied by the deposition of the most rostral one. This process is active until the primordium reaches the tip of embryo's tail and stops (i.e., until about 24 hours after the onset of migration): it eventually results in the deposition of 6-8 proto-neuromasts (named L1, L2, ..., L8), organized in a quite regular pattern along the trunk of the developing zebrafish (as sketched in Fig. 1, bottom left panel) [17, 24].

We here remark that this work is specifically focused on the description of the development of zebrafish PLL from primordium formation to the assembly of rosette L5. A sketch of PLLp configuration at this stage is reported in Fig. 1 (central left panel), according to empirical evidences in [24].

(A5) **Rosette structure and assembly.** Each rosette emerges just caudally to the previous one (except from the first one, that arises at the rostral edge of the placoid) according to the following simplified set of processes (refer again to Fig. 1, right panel). A single PM individual activates (PM $\rightarrow$ aPM) and initiates a sort of lateral inhibition mechanism that culminates in the complete three-step epithelialization (PM $\rightarrow$ dPM $\rightarrow$

pE $\rightarrow$ E) of a group of approximatively 25 cells in its surrounding, see [17, 22]. Such a phenotypic transition scheme is here assumed taking into account empirical evidences also relative to (i) the characteristic rosette morphology [9, 24], (ii) the characteristic proto-neuromasts pattern within the placode [8, 17], and (iii) the spatio-temporal evolution of SDF1a and FGF10 receptors within the body of the primordium.

(A6) **Primordium directional migration.** As already said, after the assembly of the first two/three rostral rosettes, the primordium begins to migrate along the stripe of SDF1a. Such a directional locomotion is determined by the localization and the competing activity of receptors *Cxcr4* and *Cxcr7*. A role in placode motile behavior is played also by cell-cell direct interactions (adhesion and repulsion) and by the FGF10 signaling activity, as it will be revealed by the forthcoming numerical simulations.

(A7) **Cell proliferation.** Rosette deposition reduces the number of cells forming the migrating primordium. Recalling that the placoid cluster is initially composed of nearly 100 cells and that each proto-neuromast assembly involves nearly 25 individuals, the presence of cell proliferation is therefore fundamental to have a sufficient cell mass for the formation of the physiological number (i.e., 6-8) of rosettes. In particular, according to [17], the rate of cell duplication is estimated in 2-4 mitoses/h. The same authors also observe that mitotic events are mainly located at the leading region of the PLL primordium and that they actually involve PM individuals.

3. Modeling background

Despite the importance of the biological phenomenon, probably due to the high complexity of the underlying mechanisms, only recently few mathematical models have been proposed to describe PLL embryonic development.

In [29], primordium component cells are described as 2D lattice polygons able to move towards greater concentrations of SDF1a as they express the migratory receptor *Cxcr4*. The chemical substance and its receptor are described through continuous functions, whose evolution is given by differential equations. Although the model is proposed in a 2D framework, the authors also provide and study a 1D approximation of the system. This leads to a law for the relationship between primordium speed/length and receptor dynamics and to a connection between cell proliferation (when included), placode extension and the deposition of discrete cell groups. These elegant analytic insights however derive from a necessary simplification of the biological process. For instance, critical factors as the second SDF1a-receptor *Cxcr7* and the endogenous diffusive chemicals FGF are neglected, as well as proto-neuromast differentiation and maturation.

In [7] and [8], an agent-based computational model, built in the framework of Netlogo programming environment, includes both SDF1a receptors *Cxcr4*

and *Cxcr7*. In this case, cells are represented by mobile agents, said "turtles", mutually connected by visco-elastic links, while the substrate and the source of SDF1a are described by non motile agents called "patches". The authors explore the role of SDF1a-degradation by *Cxcr4* and *Cxcr7*-expressing cells in regulating primordium locomotion and numerically reproduce several *in vivo* experiments. Their results indicate (i) that cell migration over the stripe of the exogenous chemokine is related to SDF1a concentration rather than to its gradient steepness and (ii) that there exists an additional SDF1a-independent mechanism that regulates the motion of trailing cells. This aspect is instead included in our model, which accounts for the activity of FGF10, whose signals chemotactically attract cells in the trailing region of the primordium toward those at its leading edge (which actually secrete such diffusive chemicals).

A model that takes into account the role of both SDF1a- and FGFs-related signalling pathways in regulating primordium locomotion is proposed in [1]. Therein, the cell aggregate is represented as an elliptic continuum element with embedded discrete motile individuals, that are assumed to be viscoelastic and able to undergo large deformations. At the molecular level, a system of coupled reaction-diffusion equations describes intracellular biochemical cascades involving *Cxcr4* and *Cxcr7* and the FGFs-dependent Wnt/β-catenin.

A two-dimensional hybrid model including molecular kinetics as well as rosette formation and deposition, is presented in [11]. Cells are represented as discrete entities whose motion is defined by second order-dynamic equations accounting for interagent interactions (alignment, attraction, repulsion), chemical-dependent dynamics, and damping effects. A continuous approach is conversely employed for FGFs and SDF1a signals: their spatio-temporal evolutions are in fact described by proper reaction-diffusion equations including chemokine cell internalization. The authors further consider two cell phenotypes: leader mesenchymal cells secreting FGFs and expressing *Cxcr4*, and follower epithelial cells expressing *Cxcr7* and a FGF receptor. Proper rules for leader-to-follower (i.e., mesenchymal-to-epithelial) phenotypic transition relate the process of proto-neuromast formation to the local level of the chemical substances and to lateral inhibition mechanisms. Due to the inclusion of cell transitions, the model is able to capture normal PLL development. However, this approach neglects both cell proliferation and the fact that the expression of the SDF1a-receptor *Cxcr4* is not limited to the leading cells secreting FGFs [2, 3].

Finally, a 3D hybrid model based on similar assumptions is provided in [21]: leader cells (which produce FGFs and express Wnt receptors) are there assumed to sense gradients of SDF1a, while trailing cells (which produce Wnt and express FGFs receptors) are set to be affected by gradients of FGFs. Cells are described as deformable ellipsoids of finite volume with mechano-chemical interactions (i.e., adhesion, volume exclusion, and chemokine-related active motion). The actual phenotype of a cell is then determined by the amount of Wnt/FGFs receptors expressed on its body surface. In this respect, the authors model the Wnt/FGFs signalling network, responsible for primordium separation into the leading and the trailing zone (i.e., for cell differentiation). Cell proliferation has been included as well, assuming that each individual constantly grows and

that it undergoes division after doubling its volume, thereby giving rise to two daughter cells with the same phenotype of the mother individual. Interestingly, this model is able to reproduce primordium locomotion of *wild type* embryos, as well as different behaviors observed in laser ablation experiments. However, the Wnt/FGFs subdivision is here assumed to coincide with the *Cxcr7*/*Cxcr4* partition of the primordium, a model limitation also presented in [11]. The lack of proto-neuromast formation is neglected as well.

Summing up, only in [11] the authors take into account both of primordium locomotion and of rosette formation; while all the others works focus only on different aspects of PLLp migration.

According to the assumptions introduced in Section 2, the aim of this work is conversely to provide a model (as specified in the next section) that include all the following features: the formation, maturation and deposition of proto-neuromasts; cell proliferation; both SDF1a and FGF10 signaling affecting cell motion; both SDF1a-receptors *Cxcr4* and *Cxcr7*.

4. Mathematical model

Based on the assumptions listed in the previous section, our modeling approach spans different scales. At the cellular level, a microscopic/discrete description is used for the individuals composing the primordium: it allows to reproduce their behavior, mutual interactions, and response to environmental signals. At the subcellular level, diffusive substances are described by spatial concentrations while chemical receptors by Boolean binary variables. The overall mathematical framework indeed amounts to a system of integro-differential equations for cell dynamics coupled with reaction-diffusion (RD) laws for chemical kinetics. The model is further integrated by a specific set of rules that implement cell phenotypic transitions and mitotic processes.

4.1. System representation

The substantial thinness of zebrafish embryonic body allows to deal with a bidimensional bounded domain $\Omega \subset \mathbb{R}^2$, which schematically represents the portion of the myoseptum involved in primordium migration and patterning. In particular the left border of the domain Ω represents the rostral edge of the myoseptum (close to the otic vesicle), whereas the right border of Ω indicates its caudal front (close to the tail of the embryo). Hereafter, we will focus on primordium development from its formation, occurring at $t_0 = 19$ hpf (see assumption (A1) in Section 2), to the formation of the fifth proto-neuromast, denoted by L5, occurring at $t_{\mathrm{F}} \approx 30$ hpf in wild-type embryos (see assumption (A4) in Section 2).

Each cell composing the placode is represented by a pointwise agent and labeled by an integer $i \in \{1, \dots, N(t)\}$, where $N(t)$ is the total number of individuals that may vary in time due to proliferation. The generic i-th particle is characterized by the state variable $\tau_i(t) \in \{\mathrm{PM}, \mathrm{aPM}, \mathrm{dPM}, \mathrm{pE}, \mathrm{E}\}$, which denotes its present phenotype (see Fig. 1, right panel). Its position in

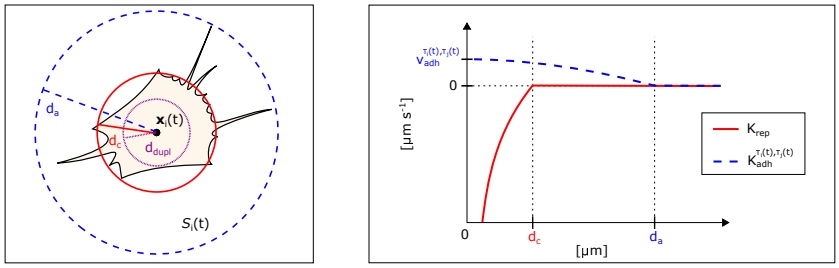

Figure 2: Left panel: Schematic representation of the morphology of the generic i-th cell, with its characteristic dimensions and sensing region $\mathcal{S}_i(t)$, as defined in Eq. (1). In particular, d_{c} denotes cell mean diameter, d_{a} is the maximal extension of plasmamembrane protrusions, and d_{dupl} a sort of perinuclear region. We also remark that phenotypic transitions does not impact on cell shapes and measures. Right panel: Plot of the repulsive kernel K_{rep} (solid line) and of the adhesive kernel $K_{\mathrm{adh}}^{\tau_i(t)\tau_j(t)}$ (dashed line), as defined in Eqs. (11) and (12), respectively.

space and velocity are instead indicated by vectors $\mathbf{x}_i(t)$ and $\mathbf{v}_i(t)$, respectively. The dimensions of the placode component cells are then taken into account by introducing three parameters: d_{c}, which is a measure of their mean diameter, d_{a}, which instead identifies the maximal extension of their plasmamembrane protrusions, and d_{dupl}, which is a sort of perinuclear diameter (obviously, $d_{\mathrm{dupl}} < d_{\mathrm{c}} < d_{\mathrm{a}}$, see Fig. 2, left panel). In this respect, for each agent i, d_{a} also defines the diameter of its actual *sensing region*:

$$\mathcal{S}_i(t) = \{\mathbf{y} \in \Omega \,:\, \|\mathbf{x}_i(t) - \mathbf{y}\| \leq d_{\mathrm{a}}/2\}\,, \tag{1}$$

i.e., a bounded round area where i is able to sense the presence of other individuals or of molecular substances, where $\|\cdot\|$ is the Euclidean norm in $\mathbb{R}^2$.

The diffusive chemicals SDF1a and FGF10 are then described by spatial concentration variables, i.e., $\sigma(t,\mathbf{x}), \varphi(t,\mathbf{x}) : [t_0, t_{\mathrm{F}}] \times \Omega \longmapsto \mathbb{R}_+$, respectively.

Finally, the intracellular presence of the specific molecular receptors is quantified, for the sake of simplicity, by Boolean variables. In particular, $c_{\tau_i(t)}$ defines if agent i, with actual phenotype $\tau_i(t)$, expresses SDF1a receptor *Cxcr4*, where

$$c_{\tau_i(t)}(t) = \begin{cases} 1, & \text{if } \tau_i(t) \in \{\text{PM, aPM, dPM}\}; \\ 0, & \text{if } \tau_i(t) \in \{\text{pE, E}\}. \end{cases} \tag{2}$$

It is useful to explicitly notice that $c_{\tau_i(t)} = 0$ implies that agent i does not express the migratory-related *Cxcr4* but rather the non migratory-related counterpart *Cxcr7* (see the right panel in Fig. 1 and the assumption (A2) in Section 2).

Coherently, $f_{\tau_i(t)}$ defines if agent i expresses FGF10 receptor *fgfr1* and reads as

$$f_{\tau_i(t)}(t) = \begin{cases} 0, & \text{if } \tau_i(t) \in \{\text{PM, aPM}\}; \\ 1, & \text{if } \tau_i(t) \in \{\text{dPM, pE, E}\}. \end{cases} \tag{3}$$

We recall that if cell i does not express *fgfr1* (i.e., if $f_{\tau_i(t)} = 0$), it produces FGF10 (see again the right panel in Fig. 1 and the assumption (A2) in Section 2).

4.2. Cell phenotypic transitions

As previously explained, the formation and stabilization of proto-neuromast structures are assumed to result from cyclical multi-step pseudo-mesenchymal-to-epithelial transitions (PM $\rightarrow$ dPM $\rightarrow$ pE $\rightarrow$ E) of localized clusters of progenitor cells, triggered by the activation of a PM individual (PM $\rightarrow$ aPM), see again Fig. 1 (right panel).

In particular, the first activation of a PM cell is set to occur at $t_1 \approx 19.1$ hpf (consistently with assumption (A4) in Section 2) and involves the agent, say i_1, located almost along the main (horizontal) axis of the primordium at a characteristic distance $l^{\mathrm{PM}\rightarrow\mathrm{aPM}}$ (empirically evaluated) from the rostral edge of the aggregate.

The following cyclical activations are delayed one from the other of a time lapse $\Delta t_k^{\mathrm{PM}\rightarrow\mathrm{aPM}}$ and involve the progenitor PMs positioned along the horizontal axis of the placode with a relative distance equal to 2 $l^{\mathrm{PM}\rightarrow\mathrm{aPM}}$ from the previously-activated individual. For instance, the generic i_k-th PM cell undergoes such a phenotypic transition at $t_k = t_{k-1} + \Delta t_k^{\mathrm{PM}\rightarrow\mathrm{aPM}}$, where $||\mathbf{x}_{i_k}(t_k) - \mathbf{x}_{i_{k-1}}(t_k)|| = 2\ l^{\mathrm{PM}\rightarrow\mathrm{aPM}}$ and $k = 2, \ldots, 5$. All these activations actually require a change in the cell state variable, i.e., $\tau_{i_k}(t_k) = \mathrm{aPM}$ for $k = 1, \ldots, 5$.

Each aPM i_k triggers (simultaneously to its state transition) the three step epithelialization of the cluster of PM cells falling within its neighborhood of radius d_{a}, defined by the set

$$\mathcal{N}_{i_k}(t_k) = \{j \in \{1, \ldots, N(t_k)\}, j \neq i_k\ :\ \tau_{i_k} = \mathrm{PM},\ \|\mathbf{x}_{i_k}(t_k) - \mathbf{x}_j(t_k)\| \leq d_{\mathrm{a}}\}. \tag{4}$$

All agents j belonging to $\mathcal{N}_{i_k}$ are indeed subjected to the following phenotypic changes: (i) at t_k, their state variable switches to dPM (i.e., $\tau_j(t_k) = \mathrm{dPM}$); (ii) then, after a characteristic time equal to $\Delta t_k^{\mathrm{dPM}\rightarrow\mathrm{pE}}$, they assume a partial epithelial fate (i.e., $\tau_j(t_k + \Delta t_k^{\mathrm{dPM}\rightarrow\mathrm{pE}}) = \mathrm{pE}$); (iii) after another delay equal to $\Delta t_k^{\mathrm{pE}\rightarrow\mathrm{E}}$, they finally acquire a fully epithelial fate (i.e., $\tau_j(t_k + \Delta t_k^{\mathrm{dPM}\rightarrow\mathrm{pE}} + \Delta t_k^{\mathrm{pE}\rightarrow\mathrm{E}}) = \mathrm{E}$). In particular the time lapse characteristic of each phenotypic transition is assumed to have a stochastic law, which accounts both for experimental measures and for the typical randomness of biological systems.

4.3. Cell proliferation

According to the assumption (A7) in Section 2, cell proliferation is relevant mainly for progenitor PM cells. Without including all details relative to the mitotic cycle, we take into account (i) of a minimum period of time between successive duplications of the same individual and (ii) of a contact-inhibition of growth in the case of high local cell density.

In this respect, starting from t_0, every $\Delta t^{\mathrm{dupl}} = 1/\gamma_{\mathrm{dupl}}$, where γ_{dupl} a mitotic rate experimentally quantified by 2-4 mitosis/h, a PM cell is randomly selected and set to undergo duplication if it is sufficiently far from other agents, i.e., if

$$d_{i,\min}(t) := \min_{\substack{j=1,\ldots,N(t)\\ j\neq i}} \|\mathbf{x}_i(t) - \mathbf{x}_j(t)\| > d_{\mathrm{dupl}}, \tag{5}$$

where, as seen, $d_{\mathrm{dupl}} < d_{\mathrm{c}}$ is a sort of cell perinuclear region. A newborn agent, labeled by the identity integer $N(t)+1$, is then added to the system close to the parent position, i.e.,

$$\mathbf{x}_{N(t)+1}(t) = \mathbf{x}_i(t) + \frac{d_c}{2} \begin{pmatrix} \cos(\eta_i(t)) \\ \sin(\eta_i(t)) \end{pmatrix}, \tag{6}$$

where $\eta_i(t)$ is a random angle uniformly distributed over $[0, 2\pi)$. The daughter cell then inherits the phenotype of its progenitor (i.e., $\tau_{N(t)+1}(t) = \tau_i(t) = \mathrm{PM}$), while its dynamics will be completely autonomous.

4.4. Cell dynamics

Cell spatial distribution evolves in time according to a set of first-order integro-differential equations, where the velocity of each individual, and not its acceleration, is assumed proportional to the acting forces. Such a relation, called *overdamped force-velocity response*, is at the basis of several discrete/IBM models (see [6, 13, 27] and references therein for further comments) and derives from the observation that cells move in extremely viscous environments characterized by a very small Reynolds number. Moreover, dealing with a planar domain, we can further neglect possible cell-cell friction contributions, as individual plasmamembranes are mainly in contact with the extracellular substrate. According to these assumptions, we can write the following law for cell motion:

$$\frac{d\mathbf{x}_i}{dt}(t) = \mu_{\tau_i(t)}(t)\, \mathbf{v}_i(t), \qquad i = 1, \ldots, N(t), \tag{7}$$

where $\mu_{\tau_i(t)}$ is a dimensionless motility coefficient that depends on the individual phenotype and takes into account also of cell-substrate friction mechanisms. In particular, we set

$$\mu_{\tau_i(t)} = \begin{cases} 1, & \text{if } \tau_i(t) \in \{\mathrm{PM,\ aPM,\ dPM,\ pE}\}; \\ 0.1, & \text{if } \tau_i(t) \in \{\mathrm{E}\}, \end{cases} \tag{8}$$

since, as explained in the assumption (A2) in Section 2, fully epithelial individuals are shown to have partially inhibited migratory ability.

The dynamics of each agent i can be then described by coupling Eq. (7) with a direct phenomenological postulation of its velocity $\mathbf{v}_i$, which can be assumed to result from the superposition of different contributions:

$$\mathbf{v}_i(t) = \mathbf{v}_i^{\mathrm{int}}(t) + \mathbf{v}_i^{\mathrm{fgf}}(t) + \mathbf{v}_i^{\mathrm{sdf}}(t) + \mathbf{v}_i^{\mathrm{rand}}(t), \qquad i = 1, \ldots, N(t). \tag{9}$$

Specifically, in Eq. (9), $\mathbf{v}_i^{\mathrm{int}}$ is the individual velocity component resulting from intercellular direct interactions (i.e., repulsive/adhesive stimuli); $\mathbf{v}_i^{\mathrm{fgf}}$ and $\mathbf{v}_i^{\mathrm{sdf}}$ instead implement cell response either to the endogenous or to the exogenous chemical, i.e., FGF10 and SDF1a, respectively, as mediated by the corresponding receptors (when expressed). Finally, $\mathbf{v}_i^{\mathrm{rand}}$ describes the random crawling typical of biological individuals.

Cell-cell interactions, $\mathbf{v}_i^{\text{int}}$. Cell-cell direct interactions include either repulsive or adhesive dynamics that are set to depend on the relative interindividual distance. Specifically, two cells tend to repel each other when they fall too close, i.e., in order to maintain a sufficient vital space. On the other hand, cell-cell adhesion arises from the activity of transmembrane molecules (cadherins): two cells can indeed form contact junctions only when their relative distance is lower than the maximal extension of their membrane protrusions. Further, we assume that both repulsive and adhesive effects on cell dynamics result from the superimposition of binary (pairwise) contributions, each aligned to the line ideally connecting the pair of interacting individuals.

In mathematical terms, we therefore have:

$$\begin{aligned}\mathbf{v}_i^{\text{int}}(t) &= \sum_{\substack{j=1\\ j\neq i}}^{N(t)} \left(\mathbf{v}_{ij}^{\text{rep}}(t) + \mathbf{v}_{ij}^{\text{adh}}(t)\right) \\ &= \sum_{\substack{j=1\\ j\neq i}}^{N(t)} \left(K_{\text{rep}}\left(\|\mathbf{r}_{ij}(t)\|\right) + K_{\text{adh}}^{\tau_i(t)\tau_j(t)}\left(\|\mathbf{r}_{ij}(t)\|\right)\right) \frac{\mathbf{r}_{ij}(t)}{\|\mathbf{r}_{ij}(t)\|},\end{aligned} \tag{10}$$

where $\mathbf{r}_{ij}(t) := (\mathbf{x}_j(t) - \mathbf{x}_i(t))$. Kernels $K_{\text{rep}} : \mathbb{R}_+ \longmapsto \mathbb{R}_-$ and $K_{\text{adh}}^{\tau_i(t)\tau_j(t)} : \mathbb{R}_+ \longmapsto \mathbb{R}_+$ model the strength of the repulsive and adhesive pairwise stimuli, respectively. Specifically, the repulsive contributions are hypothesized to be independent from the specific pair of individuals involved: biological evidence in fact does not show variations in cell repelling behavior during PLL embryonic development. On the opposite, the adhesive velocity contributions are strongly correlated to the phenotype of the interacting agents (see below). There is a wide range of kernels that satisfy the proposed model assumptions: among the possible choices, we opt for a hyperbolic-like repulsive behavior, i.e.,

$$K_{\text{rep}}(z) = \begin{cases} v_{\text{rep}}\left(1 - \dfrac{d_{\text{c}}}{z}\right), & \text{if } z \in (0, d_{\text{c}}); \\ 0, & \text{otherwise,} \end{cases} \tag{11}$$

and parabolic-like attractive dynamics, i.e.,

$$K_{\text{adh}}^{\tau_i(t)\tau_j(t)}(z) = \begin{cases} v_{\text{adh}}^{\tau_i(t)\tau_j(t)}\left(1 - \dfrac{z^2}{d_{\text{a}}^2}\right), & \text{if } z \in (0, d_{\text{a}}); \\ 0, & \text{otherwise,} \end{cases} \tag{12}$$

see Fig. 2 (right panel). In Eqs. (11)-(12), the positive coefficients v_{rep} and $v_{\text{adh}}^{\tau_i(t)\tau_j(t)}$ have speed units: in particular, v_{rep} is related to cell stiffness, while $v_{\text{adh}}^{\tau_i(t)\tau_j(t)}$ to the level (and the activity) of cell membrane adhesive proteins actually expressed by the pair of interacting individuals. In this respect, in accordance with the biological considerations listed in the previous section, we

set

$$v_{\text{adh}}^{\tau_i(t)\tau_j(t)} = \begin{cases} V_{\text{adh}}, & \text{if } \tau_i(t) = \text{aPM and } \tau_j(t) \in \{\text{dPM, pE, E}\}\text{, or viceversa;} \\ v_{\text{adh}}, & \text{otherwise,} \end{cases} \tag{13}$$

where $V_{\text{adh}} > v_{\text{adh}}$. aPM particles are in fact demonstrated to form stronger transmembrane connections to stabilize rosette bodies [25]).

FGF-dependent chemotactic velocity component, $\mathbf{v}_i^{\text{fgf}}$. The velocity component $\mathbf{v}_i^{\text{fgf}}$ implements the chemical-induced migratory signals transmitted from FGF10-producing cells (aPMs and PMs) to *fgfr1*-expressing individuals (dPMs, pEs, and Es). The intensity of such a stimulus is then assumed to depend on the amount of molecular substance perceived by agent i in its sensing region $\mathcal{S}_i$:

$$\mathbf{v}_i^{\text{fgf}}(t) = f_{\tau_i(t)}(t)\ \frac{\chi_{\text{fgf}}}{\varphi_{\max}\, A(\mathcal{S}_i(t))} \int_{\mathcal{S}_i(t)} \varphi(t, \mathbf{y})\, (\mathbf{y} - \mathbf{x}_i(t))\, d\mathbf{y}, \tag{14}$$

where $f_{\tau_i(t)}$ is the Boolean variable introduced in Eq. (3) and χ_{fgf} denotes the cell sensitivity to FGF10, whose concentration, as seen, is defined by φ. In Eq. (14), the quantity $\varphi_{\max}\, A(\mathcal{S}_i(t))$ measures the maximal amount of FGF10 that agent i can perceive within its sensing region, where $A(\mathcal{S}_i(t))$ is the actual extension of $\mathcal{S}_i(t)$ and $\varphi_{\max}$ the maximal chemical concentration experimentally found.

SDF-dependent chemotactic velocity component, $\mathbf{v}_i^{\text{sdf}}$. The velocity component $\mathbf{v}_i^{\text{sdf}}$ models the effective chemotactic locomotion along the stripe of SDF1a of *Cxcr4*-expressing cells (i.e., PMs, aPMs, and dPMs). It is set as

$$\mathbf{v}_i^{\text{sdf}}(t) = c_{\tau_i(t)}(t)\ \chi_{\text{sdf}}\ \frac{\mathbf{w}_i^{\text{sdf}}(t)}{||\mathbf{w}_i^{\text{sdf}}(t)||}, \tag{15}$$

where $c_{\tau_i(t)}$ is the binary variable introduced in Eq. (2) and χ_{sdf} denotes the strength of the cell chemotactic response. Finally, $\mathbf{w}_i^{\text{sdf}}$ defines the individual direction of movement, established by the actual SDF1a profile, i.e.,

$$\mathbf{w}_i^{\text{sdf}}(t) = \int_{\mathcal{S}_i(t)} W_i^{\text{sdf}}(t, \mathbf{y})\, \sigma(t, \mathbf{y})\, (\mathbf{y} - \mathbf{x}_i(t))\, d\mathbf{y}, \tag{16}$$

where σ is the local chemical concentration. The weight function W_i^{sdf} finally takes into account the competing effect of *Cxcr4*- and *Cxcr7*-expressing cells, since each of them sequesters a fraction of SDF1a:

$$\begin{aligned} W_i^{\text{sdf}}(t, \mathbf{y}) \quad = \Big(1 + \sum_{\substack{j=1,\\ j\neq i}}^{N(t)} \alpha_4^{\text{sdf}}\, c_{\tau_j(t)}(t)\, \mathbf{1}_{\mathcal{S}_j(t)}(\mathbf{y}) + \\ + \sum_{\substack{j=1,\\ j\neq i}}^{N(t)} \alpha_7^{\text{sdf}}\, \left(1 - c_{\tau_j(t)}(t)\right)\, \mathbf{1}_{\mathcal{S}_j(t)}(\mathbf{y})\Big)^{-1}, \end{aligned} \tag{17}$$

where $\mathbf{1}_{(\,\cdot\,)}$ is the indicator function and $\alpha_4^{\rm sdf}$, $\alpha_7^{\rm sdf} \in (0,1]$. In particular, $\alpha_4^{\rm sdf} \ll \alpha_7^{\rm sdf}$ since, as previously commented, the non migratory-related receptor *Cxcr7* has a much higher affinity with the ligand than its migratory-related counterpart *Cxcr4*. Specifically, we set $\alpha_7^{\rm sdf} = 10\alpha_4^{\rm sdf}$ consistently with assumption (A3) listed in Section 2.

Random crawling, $\mathbf{v}_i^{\rm rand}$. The typical isotropic wandering of biological individuals in the proximity of their position is finally implemented by Brownian fluctuations given, for each generic agent i, by

$$\mathbf{v}_i^{\rm rand}(t) = v_{\rm rand} \begin{pmatrix} \cos\left(\theta_i(t)\right) \\ \sin\left(\theta_i(t)\right) \end{pmatrix}, \tag{18}$$

where $\theta_i(t)$ is a random angle uniformly distributed over $[0, 2\pi)$ and $v_{\rm rand}$ is the mean speed of the primordium during migration, as measured by experimental assays.

Summing up, the phenotypic-dependent law that regulates the behavior of the i-th cell composing the primordium reads as

$$\begin{aligned} \frac{d\mathbf{x}_i}{dt}(t) \;=\; & \mu_{\tau_i(t)}(t) \Bigg[\sum_{\substack{j=1 \\ j\neq i}}^{N(t)} \Big(K_{\rm rep}\left(\|\mathbf{x}_j(t) - \mathbf{x}_i(t)\|\right) + \\ & + K_{\rm adh}^{\tau_i(t)\tau_j(t)}\left(\|\mathbf{x}_j(t) - \mathbf{x}_i(t)\|\right) \Big) \frac{\mathbf{x}_j(t) - \mathbf{x}_i(t)}{\|\mathbf{x}_j(t) - \mathbf{x}_i(t)\|} + \\ & + f_{\tau_i(t)}(t)\, \frac{\chi_{\rm fgf}}{\varphi_{\max}\, A(\mathcal{S}_i(t))} \int_{\mathcal{S}_i(t)} \varphi(t,\mathbf{y})\left(\mathbf{y} - \mathbf{x}_i(t)\right) d\mathbf{y} + \\ & + c_{\tau_i(t)}(t)\, \chi_{\rm sdf} \frac{\mathbf{w}_i^{\rm sdf}(t)}{||\mathbf{w}_i^{\rm sdf}(t)||} + \mathbf{v}_i^{\rm rand}(t) \Bigg]. \end{aligned} \tag{19}$$

From Eq. (19), it is indeed clear the integro-differential nature of the proposed model, that derives from the specific form assigned to the chemotactic velocity terms.

4.5. Chemical kinetics

According to assumption (A3) listed in Section 2, FGF10 is secreted both by progenitor PM cells and by aPM individuals at the center of each rosette-like cluster. It then diffuses in the surrounding environment and degrades at a constant rate. FGF10 kinetics are therefore described by the following reaction-diffusion equation:

$$\begin{aligned} \frac{\partial \varphi}{\partial t}(\mathbf{x},t) \;=\; & D_\varphi\, \Delta\varphi(\mathbf{x},t) + \left(1 - \frac{\varphi(\mathbf{x},t)}{\varphi_{\max}}\right) \sum_{i=1}^{N(t)} \gamma_\varphi \left(1 - f_{\tau_i(t)}(t)\right) \mathbf{1}_{\mathcal{S}_i(t)}(\mathbf{x},t) \\ & - \delta_\varphi\, \varphi(\mathbf{x},t), \end{aligned} \tag{20}$$

where D_φ and δ_φ are constant diffusion and decay coefficients, respectively. The source term implements the fact that PM and aPM cells (characterized by $f_{\tau_i(t)}(t) = 0$) produce FGF10 within their entire sensing region $\mathcal{S}_i$. The local production of the chemical has a threshold value that accounts for its present amount as well as for the maximal concentration $\varphi_{\max}$.

The stromal derived factor SDF1a is instead secreted at a constant rate over a narrow stripe $\mathcal{H} \subset \Omega$ of the horizontal myoseptum [15]. It then poorly diffuses and decays within the surrounding environment, quickly stabilizing in a quasi-homogeneous pattern. Its kinetics can be indeed described by the following reaction-diffusion equation:

$$\frac{\partial \sigma}{\partial t}(\mathbf{x}, t) = D_\sigma \, \Delta\sigma(\mathbf{x}, t) + \left(1 - \frac{\sigma(\mathbf{x}, t)}{\sigma_{\max}}\right) \gamma_\sigma \, \mathbf{1}_{\mathcal{H}}(\mathbf{x}, t) H(t - t_{\text{sdf}}) - \delta_\sigma \, \sigma(\mathbf{x}, t), \quad (21)$$

where D_σ is the diffusion coefficient, while γ_σ and δ_σ are the constant production and decay rates, respectively. In the source term in Eq. (21), the Heaviside function H is introduced to account for the experimental observation that SDF1a is detected only from $t_{\text{sdf}} = 20$ hpf (see again assumption (A3)). Also in this case, a limit over the chemical production is included. It is finally worth to notice that, in the proposed model, the evolution in time of the SDF1a distribution is completely independent from cell dynamics.

5. Numerical results

This section will first give details relative to the computational setting (e.g., the initial and the boundary conditions used for all forthcoming numerical tests) and to the definition of the critical measures used to quantify and compare model outcomes. We will then present and comment simulations that (i) describe the physiological (i.e., normal/*wild type*) development of the zebrafish PLL and (ii) reproduce several manipulations of the embryonic process, i.e., obtained by switching off selected model components.

5.1. Simulation details and quantification

As seen in the previous section, the period of observation of each simulation is given by the time interval $[t_0 = 19, t_{\text{F}} = 30]$ hpf: consistently with empirical evidence in [24], in wild-type embryos, it approximatively goes from primordium formation to the assembly of the fifth rosette L5 in wild-type embryos (see the assumptions (A1) and (A4) in Section 2). Referring to the top panel of Fig. 3, the computational domain Ω is a rectangular area of 2000×100 μm^2 that represents a section of the embryo's myoseptum where zebrafish PLL develops [10, 14, 17]. In this respect, we recall that the left and the right border of Ω computationally define the rostral and the caudal edge of the myoseptum, respectively, with the former close to the otic vesicle and the latter to the tail of the animal. The subregion $\mathcal{H}$ reproduces instead the stripe of the domain where the SDF1a is produced by the substrate: it extends over the region $[0, 2000]$ μm$\times$ $[40, 60]$ μm, in accordance with experimental measurements [10, 15].

Par.	Descr.	Val.	Ref.
$[t_0, t_F]$	period of observation	$[19, 30]$ hpf	[24]
Ω	spatial domain	$[0, 2000]$ μm $\times$ $[0, 100]$ μm	[10, 14, 17]
$\mathcal{H}$	subregion where SDF1a is produced	$[0, 2000]$ μm $\times$ $[40, 60]$ μm	[10, 15]
d_{a}	maximal extension of cell membrane protrusions	20 μm	[11]
d_{c}	mean diameter of cell body	7 μm	[17]
d_{dupl}	mean diameter of cell perinuclear region	6 μm	[17]
γ_{dupl}	PM cell proliferation rate	4 mitoses/h	[17]
Δt^{dupl}	time lapse between successive cell duplications	15 min	[17]
$l^{\mathrm{PM}\to\mathrm{aPM}}$	distance of first aPM from primordium rostral edge	16.5 μm	[24]
t_1	instant time of the first activation of a PM	19.1 hpf	[24]
$\Delta t_k^{\mathrm{PM}\to\mathrm{aPM}}$	time lapse between successive activations of PMs	$\mathcal{N}(3.07\text{ h}, 1.44\text{ h})$	[18, 22, 24]
$\Delta t_k^{\mathrm{dPM}\to\mathrm{pE}}$	time lapse between PM deactivation and its partial epithelialization	$\mathcal{N}(4.2\text{ h}, 1.12\text{ h})$	[18, 22, 24]
$\Delta t_k^{\mathrm{pE}\to\mathrm{E}}$	time lapse between partial and full epithelialization of a cell	$\mathcal{N}(4\text{ h}, 1.17\text{ h})$	[18, 22, 24]
D_φ	diffusion coefficient of FGF10	10 $\mu\mathrm{m}^2\,\mathrm{s}$	[21]
$\varphi_{\max}$	maximal concentration of FGF10	1.5 nM	[21]
δ_φ	FGF10 decay rate	$0.0025\ \mathrm{s}^{-1}$	[21]
γ_φ	FGF10 secretion rate	$0.0083\ \mathrm{nM\,s}^{-1}$	[21]
D_σ	diffusion coefficient of SDF1a	$0.333\ \mu\mathrm{m}^2\,\mathrm{s}^{-1}$	[21]
$\sigma_{\max}$	maximal concentration of SDF1a	0.5 nM	[21]
δ_σ	SDF1a decay rate	$0.0033\ \mathrm{s}^{-1}$	[21]
γ_σ	SDF1a secretion rate	$0.0033\ \mathrm{nM\,s}^{-1}$	[21]
t_{sdf}	instant time of SDF1a onset	20 hpf	[21]
v_{rand}	mean speed of the primordium	$0.019\ \mu\mathrm{m\,s}^{-1}$	[22]
v_{rep}	strength of repulsive interactions	$10\ \mu\mathrm{m\,s}^{-1}$	data fitting
v_{adh}	strength of adhesive interactions ($v_{\mathrm{adh}}/v_{\mathrm{rep}} = 0.005$ [4, 5, 6, 26])	$0.05\ \mu\mathrm{m\,s}^{-1}$	data fitting
V_{adh}	strength of overadhesive interactions ($V_{\mathrm{adh}} = 2v_{\mathrm{adh}}$ [21])	$0.1\ \mu\mathrm{m\,s}^{-1}$	data fitting
χ_{fgf}	level of activity of FGF10 receptor *fgfr1*	$0.1\ \mu\mathrm{m}^2\,\mathrm{s}^{-1}$	data fitting
χ_{sdf}	level of activity of SDF1a receptor *Cxcr4*	$0.1\ \mu\mathrm{m}^2\,\mathrm{s}^{-1}$	data fitting
α_4^{sdf}	affinity of receptor *Cxcr4* for its ligand SDF1a	0.05	data fitting
α_7^{sdf}	affinity of receptor *Cxcr7* for its ligand SDF1a ($\alpha_7^{\mathrm{sdf}} = 10\alpha_4^{\mathrm{sdf}}$ [9])	0.5	data fitting

Table 1: List of model parameters. $\mathcal{N}(\mu, s)$ denotes a Gaussian distribution characterized by mean μ and variance s.

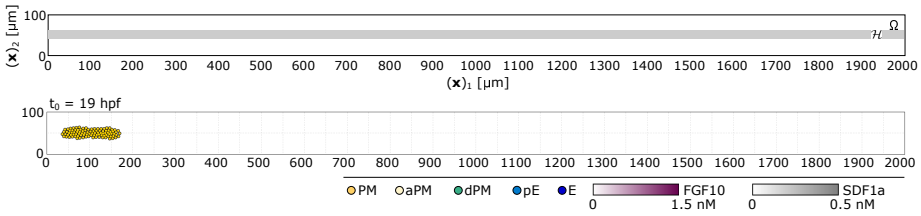

Figure 3: Simulation setting. Top panel: Plot of the computational domain Ω used in all numerical simulations. The grey area denotes the subregion $\mathcal{H}$ where the SDF1a is produced. Bottom panel: Initial configuration of the placode aggregate, i.e., at $t_0 = 19$ hpf, which will be the same for all realizations. In particular, the yellow disks, which have a diameter equal to d_c, represent the $N(t_0) = 100$ PM component individuals.

The domain boundary $\partial\Omega$ is then assumed to be a physical barrier for the computational system since it reproduces the wall of somites that encloses the myoseptum of the animal. Since this type of cells has the capacity to internalize FGF10 but not SDF1a, we provide Eq. (20) with a homogeneous Dirichlet condition, i.e., $\varphi(\mathbf{x}) = 0$ on $\partial\Omega$, and Eq. (21) with a no-flux Neumann law, i.e., $\partial_{\mathbf{n}(\mathbf{x})}\sigma(\mathbf{x}) = 0$ on $\partial\Omega$, where $\mathbf{n}(\mathbf{x})$ the outgoing unit vector applied at the domain border point $\mathbf{x}$. Finally, Eq. (7) is equipped by proper algorithmic rules that prevents cell bodies from crossing the edge of Ω.

We finally assume that at the initial time instant $t_0 = 19$ hpf, there are no chemicals in the system, i.e., $\varphi(\mathbf{x}, t_0) = \sigma(\mathbf{x}, t_0) = 0$ for any $\mathbf{x} \in \Omega$, while the primordium is an ellipsoidal cluster (with horizontal axis ≈ 135 μm) constituted by $N(t_0) = 100$ PM individuals located at the rostral (left) edge of the domain, see Fig. 3 (bottom panel). Such an initial placode morphology is consistent with the empirical images reported, among others, in [17].

The development of the primordium is hereafter quantified by evaluating (i) its horizontal extension at the onset of the effective migration which is calculated as

$$E_{\mathrm{PLL}} := \max_{\substack{i,j=1,\dots,N(\widetilde{t}\,)\\ i\neq j}} \left|(\mathbf{x}_i)_1(\widetilde{t}\,) - (\mathbf{x}_j)_1(\widetilde{t}\,)\right|, \tag{22}$$

where, according to assumption (A6) in Section 2, $\widetilde{t}$ is the instant time of the partial epithelialization of the first-formed rosette L1 (i.e., of the dPM $\rightarrow$ pE transition that leads to the earliest expression of the receptor *Cxcr7*); and (ii) its mean directional speed, which is measured as the mean velocity of the caudal edge during the effective migration, as

$$v_{\mathrm{PLL}} := \frac{1}{(t_{\mathrm{F}} - \widetilde{t}\,)} \left| \max_{i=1,\dots,N(t_{\mathrm{F}})} (\mathbf{x}_i)_1(t_{\mathrm{F}}) - \max_{i=1,\dots,N(\widetilde{t}\,)} (\mathbf{x}_i)_1(\widetilde{t}\,) \right|. \tag{23}$$

In Eqs. (22)-(23), $(\mathbf{x}_i)_1$ denotes the horizontal coordinate of the cell actual position. These two measures have been used for parameter estimate, as discussed in details in Appendix A. The complete list of model coefficients is finally given in Tables 1.

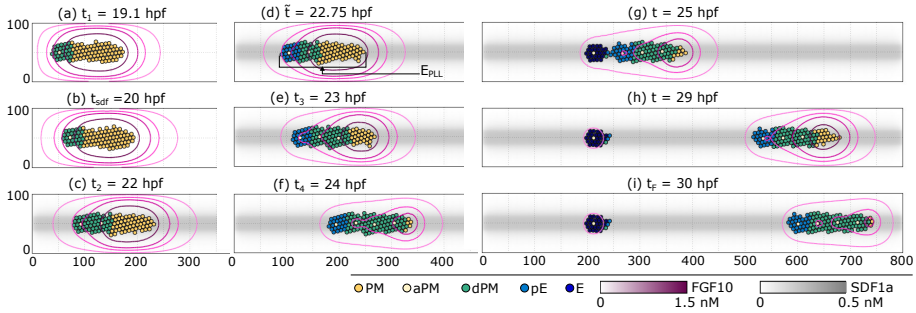

Figure 4: Reference simulation. Time-lapse images of the evolution of the computational primordium from its formation at $t_0 = 19$ hpf to $t_F = 30$ hpf, i.e., which approximately coincides with the formation of the fifth rosette in wild-type embryos. In all panels, cells are represented as rigid disks with diameter equal to d_c whose color denotes their actual phenotype. The distribution of FGF10 is instead represented through contour level curves (corresponding to $\varphi = 0.05, 0.15, 0.25, 0.5$, respectively), while the local amount of SDF1a is plotted in grey. For visualization purposes, in each panel, we only show the subregion of the domain that fully contains the primordium.

5.2. Reference simulation

The reference simulation is based on the full model introduced in Section 4. It qualitatively and quantitatively reproduces the physiological early development of the zebrafish PLL and plays also the role of benchmark test for the parametric estimate described in Appendix A.

A representative realization of the evolution of the *wild-type* primordium is given in Fig. 4, where in each panel we show the portion of the domain actually containing the cell aggregate. At $t_1 = 19.1$ hpf, see Fig. 4 (a), a PM individual in the rostral part of the placode cluster differentiates and induces the deactivation of the cells in its surrounding, which in turn form the proto-neuromast named L1. The primordium then slightly shifts towards the embryo's tail, see Fig. 4 (b), consistently with empirical results in [24]. This phenomenon is mainly due to the fact that *fgfr1*-expressing dPM cells forming the rosette L1, located at the rostral edge of the aggregate, are chemotactically attracted towards FGF10-producing PM individuals and push them forward (i.e., towards the caudal edge of myoseptum).

At $t_{\text{sdf}} = 20$ hpf, the exogenous SDF1a starts to be produced by the substrate and the placode elongates accordingly, see Fig. 4 (c). This phenomenology, experimentally observed in [9, 24], is due to the fact that both the dPM individuals forming the rosette at the trailing edge of the proto-organ, and the PM agents constituting the rest of the placode, express the migratory-related receptor *Cxcr4*. As a consequence, the rostral and the caudal areas of the primordium concomitantly tend to extend along the SDF1a stripe in opposite directions: such competing forces impede an effective locomotion of the aggregate as well.

At $t_2 = 22$ hpf a second rosette (L2) assemblies just caudally to the first one, see again Fig. 4 (c), which in turn undergoes partial epithelialization at

$\widetilde{t} = 22.75$ hpf, see Fig. 4 (d). As a consequence, the primordium begins to actively migrate: the cells forming proto-neuromast L1 in fact acquire a pE phenotype and no longer express the SDF1a-receptor *Cxcr4* but the non-migratory counterpart *Cxcr7*. Only the caudal part of the primordium therefore remains subjected to the SDF1a-induced velocity contribution: it is indeed free to advance within the myoseptum where it is also able to drag the rest of the placode (consistently with the assumption (A6) in Section 2).

During migration, further additional rosettes sequentially form towards the caudal region of the aggregate, see Fig. 4 (e)-(f). After the assembly of the fourth proto-neuromast (named L4), the pE particles forming the most rostral rosette L1 undergo full epithelialization (since the time-lapse needed for the corresponding phenotypic transitions has passed by), see Fig. 4 (g). This results in a drop of their migratory ability and causes the arrest of the entire proto-neuromast, which separates form the rest of the placode and is then deposited within the myoseptum, see Fig. 4 (h). This process is also promoted by the intrinsic compactness of the rosettes due to the enhanced adhesiveness of the central aPM agent and to FGF10-signaling.

After the deposition of proto-neuromast L1, the placode aggregate, that now comprises rosettes L2, L3 and L4, as well as the remaining group of PM agents, continues to actively migrate towards the embryo's tail. At $t_{\mathrm{F}} = 30$ hpf, we finally observe the formation of the fifth rosette (L5), see Fig. 4 (i). The cyclical dynamics characteristic of the proto-organ, will then start and amount in a sequence of proto-neuromast depositions from the rostral edge of the migrating placode and rosette assemblies at its caudal area. However, we will not focus on this second phase.

The effective directional movement of the primordium is the result of two mechanisms:

- on one hand, *Cxcr4*-expressing cells, mainly located at the caudal region of the placode, drag by adhesion *Cxcr7*-expressing individuals which, as seen, are mainly located at the rostral area of the aggregate being the components of the (partially or fully) epithelialized rosettes;

- on the other hand, *fgfr1*-expressing cells (i.e., dPM, pE and E agents), that compose proto-neuromast bodies and therefore are mainly located at the rostral region of the placode, are chemotactically attracted towards FGF10-producing individuals, mainly present at the caudal region of the aggregate, and therefore push them forward along the myoseptum also thank to repulsive responses.

From this analysis, we can affirm that FGF10 not only has a stabilizing effect (in addition to adhesive interactions) within each rosette structure, but also sustains the coordinated directional migration of the aggregate.

It is useful to notice that the model ability to qualitatively reproduce the PLL embryonic development relies both on the accurate estimate (in terms of mean and variance) of the characteristic times of progenitor cell activation and individual epithelialization and on the inclusion of duplication mechanisms

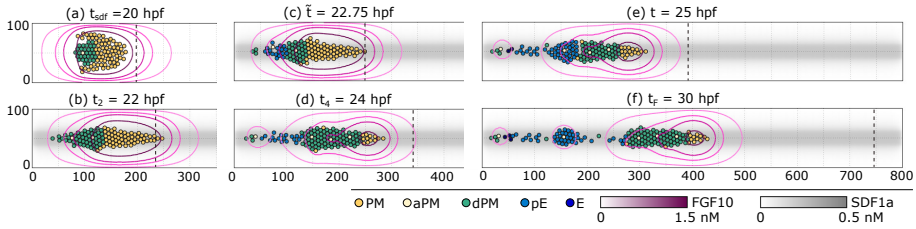

Figure 5: Effect on primordium evolution of disruption of cell-cell adhesion, i.e., obtained by setting $v_{\mathrm{adh}}^{\tau_i(t)\tau_j(t)} = 0\ \mu\mathrm{m\,s}^{-1}$ for any $i, j = 1, \ldots, N(t)$ and $t \in [t_0, t_{\mathrm{F}}]$ in Eq. (13). For visualization purposes, each panel shows only the subregion of the domain that fully contains the primordium. For comparison purposes, at each considered time instant, a dashed black line denotes the position of primordium caudal edge observed in the reference simulation.

(needed to maintain a sufficient amount of cells). We finally remark that, thanks to a proper parameter estimate, the results of the simulations are also quantitatively coherent with the corresponding experimental evidences, in terms of both placode elongation at the onset of migration (triggered by the partial epithelialization of the first formed rosette occurring at $\widetilde{t} = 22.75$ hpf) and mean speed, since $E_{\mathrm{PLL}} = 158 \in [140, 175]\ \mu$m (as stated in assumption (A2)), and $v_{\mathrm{PLL}} = 0.019 \in [0.018, 0.019]\ \mu\mathrm{m\,s}^{-1}$ (as estimated in [22]), see the Appendix for further details.

5.3. Experimental manipulations and corresponding numerical analysis

We now turn to present several simulations that will reproduce selected experimental manipulations of the normal PLL development. Specifically, in each case, we will start from the initial condition of the reference setting introduced in Sections 5.1 and give details on the model modifications. Table 2 will then summarize, for comparison purposes, the values of the primordium elongation at the onset of migration, i.e., E_{PLL} and of mean speed, i.e., v_{PLL} obtained either in the reference simulation or in the case of model perturbations. In this perspective, for comparison purposes, all the forthcoming simulations will be performed by fixing both the period of observation $[t_0, t_{\mathrm{F}}]$ and the time lapses between subsequent differentiations, i.e., $\Delta t_k^{\mathrm{PM}\to\mathrm{aPM}}$, $\Delta t_k^{\mathrm{dPM}\to\mathrm{pE}}$ and $\Delta t_k^{\mathrm{pE}\to\mathrm{E}}$ with $k = 1, \ldots, 5$, as in reference simulation described in Section 5.2 and reported in Fig. 4.

Inhibition of cell-cell adhesion. In order to analyze the role played by cell-cell adhesive contributions, we assume $v_{\mathrm{adh}}^{\tau_i(t)\tau_j(t)} = 0\ \mu\mathrm{m\,s}^{-1}$ in Eq. (13), for any pair of agents $i, j = 1, \ldots, N(t)$ and for any $t \in [t_0, t_{\mathrm{F}}]$, so that cell dynamics are only regulated by repulsive interactions, chemical signals and randomness.

Before SDF1a enters the picture, this knock-out results in an horizontal compression/vertical enlargement of the aggregate, see Fig. 5 (a). The underlying rationale relies on the following mechanism: the *fgfr1*-expressing cells composing the rostral rosette L1 are chemotactically attracted towards the FGF10-secreting PM individuals located at the caudal region of the primordium; such

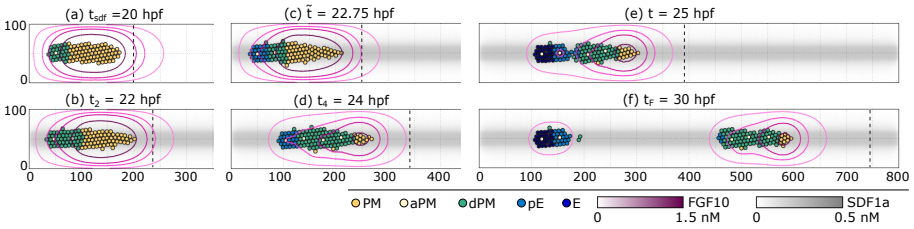

Figure 6: Effect on primordium evolution of disruption of the activity of FGF10-receptor *fgfr1*, i.e., obtained by setting $\chi_{\mathrm{fgf}} = 0\ \mu\mathrm{m}^2\mathrm{s}^{-1}$ in Eq. (14). For visualization purposes, each panel shows only the subregion that actually contains the primordium. For comparison purposes, at each considered time instant, a dashed black line denotes the position of primordium caudal edge observed in the reference simulation. Analogous system behavior is observed by setting $\gamma_\varphi = 0\ \mathrm{nM\,s}^{-1}$ in Eq. (20), i.e., by inhibiting FGF10 production.

PMs are only subjected to repulsive interactions and random motility: therefore, they scatter and engulf the proto-neuromast, rather than be compactly pushed forward as in the reference case.

As soon as the stripe of SDF1a is formed, the primordium morphology completely changes, see Fig. 5 (b): we observe in fact a substantial horizontal stretch and a vertical contraction of the placode (that finally result in $E_{\mathrm{PLL}} = 210\ \mu\mathrm{m}$, see Fig. 5 (c)). This phenomenon is due to the fact that, in the absence of intercellular adhesions, the *Cxcr4* expressing individuals at both the caudal and the rostral edges of the aggregate are more free to move along the stripe of SDF1a. This somewhat dispersed elongation in turn leaves enough space for the cells located at the upper and at the bottom regions of the primordium, that also have *Cxcr4*, to crawl towards the central SDF1a-producing domain stripe.

The absence of intercellular adhesion also affects the subsequent evolution of the primordium. In fact, proto-neuromast assembly and maturation are disrupted, since a trail of isolated cells or of small groups of cells emerges at rostral edge of the migrating primordium. Specifically, in the lack of adhesive interactions, partially epithelialized rosettes detach from the rest of placode and progressively disassembly (see the firstly-formed rosette in Fig. 5 (c)-(d) and rosette L2 in Fig. 5 (e)-(f)). The overall directional velocity is significantly reduced as well, as $v_{\mathrm{PLL}} = 0.007\ \mu\mathrm{m\,s}^{-1}$. This is probably due to the fact that, in the absence of direct adhesion forces, the leader *Cxcr4*-expressing individuals can drag the remaining cell mass only by FGF10 signaling, see Fig. 5 (f).

From such a simulation setting, we can conclude that, in our model, *cell-cell adhesion is crucial to preserve the normal compact morphology of proto-neuromasts and of the primordium at different stages of its early development, contributing also to promote its efficient migration.*

Disruption of FGF10 signaling pathways. In order to investigate the role of FGF10 signaling in primordium dynamics, we first set $\chi_{\mathrm{fgf}} = 0\ \mu\mathrm{m}^2\mathrm{s}^{-1}$ in Eq. (14), which experimentally corresponds to the inhibition of the activity of receptor *fgfr1*. Cell dynamics are therefore regulated by cell-cell repulsive/adhesive interactions and by the SDF1a-related velocity component, in

conjunction with random motility.

As shown in Fig. 6 (a), the model perturbation prevents the initial (i.e., occurring before SDF1a production) displacement of the primordium observed in the reference case, thereby confirming that this phenomenon is regulated by FGF10-signaling, cf. with Fig. 4 (a)-(b). After the appearance of the exogenous chemical, see Fig. 6 (b), the placode excessively stretches along the horizontal axis (as quantified by $E_{\mathrm{PLL}} = 178$ μm, see Fig. 6 (c)), probably as the consequence of the lack of the stabilizing effect of FGF10.

The aggregate then starts to crawl towards the caudal region of the myoseptum as soon as the first rosette (L1) undergoes partial epithelialization, see Fig. 6 (c). However, its migration is dramatically altered, being characterized by a decreased directional motility (as $v_{\mathrm{PLL}} = 0.015$ $\mu\mathrm{m\,s}^{-1}$), see Fig. 6 (d)-(f). This is due to the fact that, in the absence of FGF10-signaling cues, the *fgfr1*-expressing cells composing the rosettes are no longer chemotactically attracted by the PM individuals at the leading/caudal region of the PLL. pE and E particles can be indeed only passively dragged via adhesive interactions, since they express the non-migratory receptor *Cxcr7*, thereby slowing down the entire primordium.

Such an abnormal movement also affects proto-neuromast patterning. As shown in Fig. 6 (e)-(f), the immature rosette L2 is in fact not able to follow the locomotion of the leading part of the aggregate along the SDF1a stripe but it rather remains anchored to the fully epithelial proto-neuromast L1.

However, we do not observe alteration in rosette compactness, w.r.t the reference simulation. In this respect, we can speculate that *in our model FGF10 activity is mainly implicated in primordium migration and patterning rather than in proto-neuromast organization. Intercellular adhesion (characterizing, in particular, the central aPM) seems to be in fact sufficient to maintain the stabilization of the assembled rosettes.*

An analogous phenomenology is observed if we block FGF10 production, i.e., by setting $\gamma_{\varphi} = 0$ $\mathrm{nM\,s}^{-1}$ in Eq. (20), so that $\varphi(\mathbf{x}, t) = 0$ for any $\mathbf{x} \in \Omega$ and $t \in [t_0, t_F]$ (not shown).

A drop in primordium directional velocity upon disruption in FGF10-related pathways has been reported also in [22, 24], where experimental manipulations affected either the normal production of the chemical or the activity of its cell surface receptors. However, in these empirical *assays*, the authors observed also the inhibition of rosette assembly and the disaggregation of the already formed immature proto-neuromasts. Such a discrepancy with the proposed model results may be due to the fact that FGF10 signaling cascades are somehow implicated in cell phenotypic transitions as well, an aspect not included in the present version of our approach and that needs further experimental investigation.

Disruption of SDF1a migratory signaling pathways. In order to analyze the role played by SDF1a in PLL embryonic evolution, we first inhibit the activity of the migratory related receptor *Cxcr4*, by setting $\chi_{\mathrm{sdf}} = 0$ $\mu\mathrm{m}^2\mathrm{s}^{-1}$ in Eq. (16). Cell dynamics are indeed regulated by repulsive/adhesive intercellular interactions, FGF10 signals, and randomness.

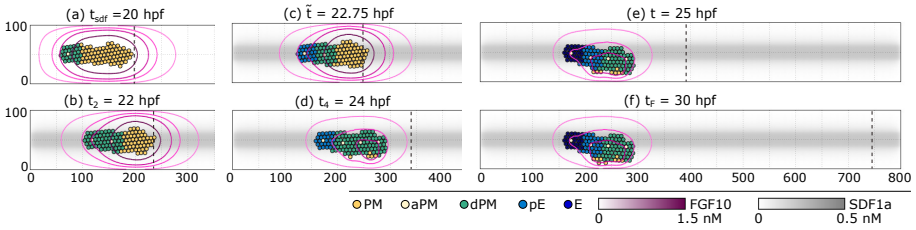

Figure 7: Effect on primordium evolution of disruption of the activity of SDF1a-receptor *Cxcr7*, i.e., obtained by setting $\chi_{\text{sdf}} = 0\ \mu\text{m}^2\text{s}^{-1}$ in Eq. (16). For visualization purposes, each panel shows only the subregion that actually contains the primordium. For comparison purposes, at each considered time instant, a dashed black line denotes the position of primordium caudal edge in the reference simulation. An analogous behavior of the placode results by setting $\gamma_\sigma = 0\ \text{nM}\,\text{s}^{-1}$, in Eq. (21) by inhibiting SDF1a production.

As shown in Fig. 7, the consequence of the proposed model manipulation is the complete disruption of the normal primordium development. First, the placode aggregate normally moves forward driven by FGF10 signals, cf. Fig. 7 (a) with Fig. 4 (a)-(b), but it then does not stretch along the stripe of SDF1a w.r.t. the reference case (as quantified by $E_{\text{PLL}} = 133\ \mu\text{m}$), since its individuals are insensitive to the exogenous chemical only, see Fig. 7 (b)-(c). Then the placode only slightly moves from its initial position due to randomness and to the pushing forces that *fgfr1*-expressing cells, which form the rosettes in the rostral region of the aggregate, exert on the FGF10-secreting PM individuals located at the caudal area, as quantified by $v_{\text{PLL}} = 0.001\ \mu\text{m}\,\text{s}^{-1}$ and shown in Fig. 7 (d)-(f). Finally, the absence of the SDF1a-driven chemotactic migration does not allow a correct proto-neuromast formation and deposition as well: the mature rosette L1 in fact remains attached to the rest of the aggregate body, see Fig. 7 (e), and the lack of PM individuals, due to the fact that their normal proliferation is inhibited by an extreme compactness of the placode, avoids the assembly of the fifth rosette, see Fig. 7 (f).

This simulation setting highlights that *FGF10 signals are implicated in primordium migration* (consistently with the outcomes of the previous numerical simulation), *but they are not able, in the absence of SDF1a signals, to sustain the normal displacement of the primordium.* Moreover, it emerges that, in our model, *SDF1a signals are involved in the initial stretching of the placode and in the maintenance of its typical elongated morphology, which is crucial to allow normal proto-neuromasts formation and deposition.*

Almost the same behavior, with some differences due to randomness in cell dynamics and proliferation, is observed in the case of inhibition of SDF1a production by the substrate, i.e., obtained by setting $\gamma_\sigma = 0\ \text{nM}\,\text{s}^{-1}$, in Eq. (21), so that $\sigma(\mathbf{x}, t) = 0$ for any $\mathbf{x} \in \Omega$ and $t \in [t_0, t_F]$ (not shown).

The absence of SDF1a signaling, obtained by inhibiting either *Cxcr4* expression/activity or ligand production, has been shown to results in a rounder and more compact morphology of the primordium, accompanied to a dramatic drop its directional movement also experimentally, see [15, 18].

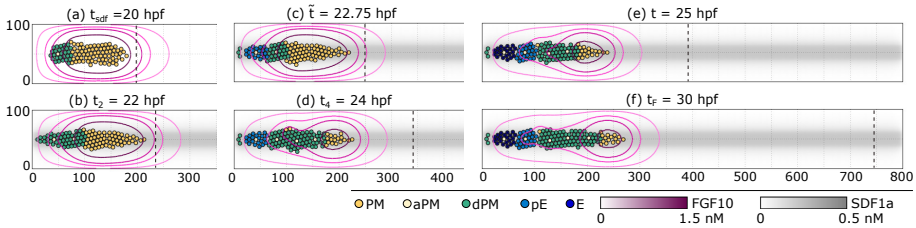

Figure 8: Evolution of primordium evolution in the case of inhibited activity both of cell-cell adhesive molecules and of *fgfr1* receptors, computationally obtained by assuming $v_{\text{adh}}^{\tau_i(t)\tau_j(t)} = 0\ \mu\text{m}\,\text{s}^{-1}$ for any $i, j = 1, \ldots, N(t)$ at any $t \in [t_0, t_F]$ in Eq. (13), and $\chi_{\text{fgf}} = 0\ \mu\text{m}^2\text{s}^{-1}$ in Eq. (14). For visualization purposes, only a subregion that actually contains the primordium is shown. For comparison purposes, at each considered time instant, a dashed black line denotes the position of primordium caudal edge in the reference simulation.

Simultaneous inhibition of cell-cell adhesion and of FGF10 signaling pathways. We then turn to analyze primordium behavior obtained by simultaneously neglecting cell-cell adhesion and FGF10-signaling, i.e., by setting $v_{\text{adh}}^{\tau_i(t)\tau_j(t)} = 0\ \mu\text{m}\,\text{s}^{-1}$ for any $i, j = 1, \ldots, N(t)$ and $t \in [t_0, t_F]$ in Eq. (13), and $\chi_{\text{fgf}} = 0\ \mu\text{m}^2\text{s}^{-1}$ in Eq. (14). Cell dynamics result indeed regulated only by repulsive interactions, SDF1a-related chemotaxis and randomness.

As shown in Fig. 8, the primordium initially does not move forward due to FGF10 signaling, see Fig. 8 (a), and is more elongated than its *wild type* counterpart, see Fig. 8 (b)-(c) (specifically, we have $E_{\text{PLL}} = 209\ \mu\text{m}$). Its directional speed is then dramatically reduced, as $v_{\text{PLL}} = 0.002\ \mu\text{m}\,\text{s}^{-1}$, see Fig. 8 (d)-(f). This behavior is due to the redundant effects of the two model manipulations: both have been in fact shown to have the same consequences on primordium development, cf. Figs. 5 and 6 and see Table 2.

Figure 8 also shows that rosette-like structures form and mature but are characterized by a low inner compactness. Such a phenomenology mainly relies on the absence of intercellular adhesion since we have previously observed that the inhibition of FGF10 signaling does not significantly impact on the morphology of the single proto-neuromasts (and therefore of the entire aggregate).

Summing up, this simulation setting allows to claim that *the SDF1a-related velocity contribution is responsible for primordium initial stretching* (according to the previous simulation), *but is not sufficient to dictate a directional displacement of the primordium.* In this respect, we can speculate that *SDF1a signaling has to be accompanied at least by the activity of cell-cell adhesion molecules to drive a coordinated migration of the aggregate*, cf. Figs. 6 and 8.

Simultaneous inhibition of cell-cell adhesion and of SDF1a migratory signaling pathways. The disruption in intercellular adhesiveness is now coupled with the inhibition of SDF1a signaling, here obtained by interfering with the activity of its migratory related receptor *Cxcr4*, computationally implemented by setting $\chi_{\text{sdf}} = 0\ \mu\text{m}^2\text{s}^{-1}$ in Eq. (16). Cell dynamics are indeed established by repulsive interactions, FGF10-dependent chemical cues and random crawling.

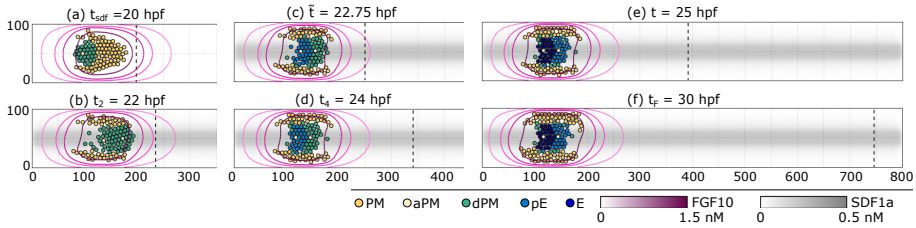

Figure 9: Evolution of primordium in the case of disruptions both in cell-cell adhesion and in activity of *Cxcr4* receptors, i.e., obtained by assuming $v_{\text{adh}}^{\tau_i(t)\tau_j(t)} = 0\ \mu\text{m}\,\text{s}^{-1}$ for any $i, j = 1, \dots, N(t)$ and $t \in [t_0, t_{\text{F}}]$ in Eq. (13), and $\chi_{\text{sdf}} = 0\ \mu\text{m}^2\text{s}^{-1}$ in Eq. (16), respectively. For visualization purposes, only a subregion that actually contains the primordium is shown. For comparison purposes, at each considered time instant, a dashed black line denotes the position of primordium caudal edge in the reference simulation.

As shown in Fig. 9, the primordium quickly acquires a rounded configuration (characterized by $E_{\text{PLL}} = 116\ \mu\text{m}$), where the two assembled proto-neuromasts stabilize as a central bulk surrounded by a incomplete ring of with PM individuals. The underlying rationale is that *fgfr1*-expressing cells forming the body of the rosettes are chemotactically attracted both by the aPM at the center of each cluster and by the PM agents that are initially located at the caudal region of the placode, see Fig. 9 (a)-(c). Therefore, only an engulfed configuration is able to maximize such competing stimuli. In fact, PM individuals, which are neither subjected to adhesion nor to SDF1a signals, are free to scatter and relocate above or below proto-neuromast bodies which in turn are kept somehow more compact by FGF10 signals, transmitted by the central aPM to the surrounding individuals.

The placode eventually crawls around its initial position (as quantified by $v_{\text{PLL}} = 1.4 \cdot 10^{-4}\ \mu\text{m}\,\text{s}^{-1}$ and shown in Fig. 9 (d)-(f)). Primordium pathological morphology and movement also inhibit the formation of the correct number of rosettes, see again Fig. 9.

This simulation setting allows us to observe that also *the FGF10-related velocity contributions are not sufficient to drive a compact displacement of the primordium. They conversely have to be coupled with a feature that is able to preserve a minimal cohesion of the placode* (i.e., the activity of cell-cell adhesion molecules, cf. Fig. 5 and 9, or SDF1a-dependent cell dynamics, cf. Figs. 5 and 7) *to result in a coordinated migration of the aggregate.*

Inhibition of cell proliferation. As stated in the assumption (A7), the loss of cell mass due to rosette deposition is partially compensated by mitotic processes [17]. In order to highlight the crucial role of cell proliferation in PLL development, we indeed analyze the model outcomes in the absence of duplication of PM individuals, obtained by assuming $\gamma_{\text{dupl}} = 0$ mitoses/h.

As expected, and shown in Fig. 10, *the inhibition of mitotic events disrupts the normal formation of rosettes.* After the assembly of the fourth proto-neuromast, the placode in fact remains completely deprived of PM individuals and the fifth rosette can no longer form, see Fig. 10 (d).

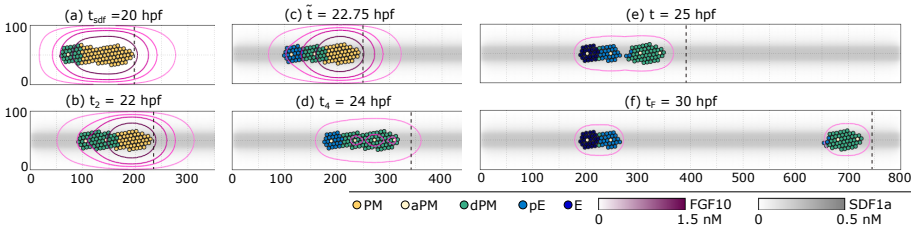

Figure 10: Primordium development in the absence of cell proliferation, i.e., obtained by setting $\gamma_{\text{dupl}} = 0$ mitoses/h. For visualization purposes, each panel shows only the subregion of the domain that fully contains the primordium. For comparison purposes, at each considered time instant, a dashed black line denotes the position of primordium caudal edge in the reference simulation.

Simulation setting	E_{PLL}	v_{PLL}
References simulation	158 μm	0.019 $\mu\text{m}\,\text{s}^{-1}$
Inhibition of cell-cell adhesion	210 μm	0.007 $\mu\text{m}\,\text{s}^{-1}$
Disruption of FGF10 signaling pathways	178 μm	0.015 $\mu\text{m}\,\text{s}^{-1}$
Disruption of SDF1a signaling pathways	133 μm	0.001 $\mu\text{m}\,\text{s}^{-1}$
Simultaneous inhibition of cell-cell adhesion and of the activity of receptor *fgfr1*	209 μm	0.002 $\mu\text{m}\,\text{s}^{-1}$
Simultaneous inhibition of cell-cell adhesion and of the activity of receptor *Cxcr4*	116 μm	$1.35 \cdot 10^{-4}$ $\mu\text{m}\,\text{s}^{-1}$
Inhibition of cell proliferation	143 μm	0.018 $\mu\text{m}\,\text{s}^{-1}$

Table 2: Values of the initial elongation of the primordium, E_{PLL}, and of its directional mean speed, v_{PLL}, defined in Eqs. (22) and (23), respectively, as obtained either in the reference simulation in Section 5.2 or in the cases of the model manipulations proposed in Section 5.3. We remark that admissible values are given by the ranges $E_{\text{PLL}} \in [140, 175]$ μm and $v_{\text{PLL}} \in [0.018, 0.019]$ $\mu\text{m}\,\text{s}^{-1}$, in accordance to the empirical measures provided in [17, 22].

The absence of cell proliferation also results in an abnormal fragmentation of the migrating placode, see Fig. 10 (e)-(f): the immature rosette L2 in fact remains attached to the mature proto-neuromast L1 and separates from the rest of the aggregate. This is probably due to the decreased number of FGF10-producing PM individuals at the caudal region of the placode, which are insufficient to chemotactically drag the trailing rosette L2. Such an hypothesis is supported by the fact that an analogous behavior has been obtained in case of disruption in the FGF10-related signaling pathways, cf. with Fig. 6 (e)-(f).

Interestingly, disruption of cell duplication does not have a significant effect on the initial elongation of the primordium and on its mean directional speed, since the corresponding values still fall within the range of the physiological measures (i.e., $E_{\text{PLL}} = 143$ μm and $v_{\text{PLL}} = 0.018$ $\mu\text{m}\,\text{s}^{-1}$).

6. Conclusions

In this work, we have proposed a model able to capture normal and abnormal early development of zebrafish PLL. The cell aggregate has been described as a set of interacting particles whose behavior has been then assumed to depend on their actual phenotype. Each cell has been characterized also by a region

of perception and by the expression of specific receptors, in turn described by Boolean binary variables. The diffusive chemicals (SDF1a and FGFs) have been finally represented through proper spatial distributions. This has lead to a hybrid model. Cell dynamics have been in fact regulated by first-order integro-differential equations where non-local differential terms reproduce cell-cell direct interactions (adhesion/repulsion), while integral velocity components implement FGF10- and SDF1a-related dynamics. Specifically, proper weight functions have been included in the integrals in order to take into account that a local fraction of chemical substances can be temporarily not available for a given cell since it may be actually sequestered by surrounding individuals. Finally, proper rules have been included to implement cell duplication and phenotypic transitions.

The proposed approach has been able to capture both qualitatively and quantitatively the *wild-type* development of PLL, in terms of morphology, migratory characteristics, and dynamics of proto-neuromast assembly and deposition. Moreover, several manipulations of the system have been investigated in order to analyze the consistency of the model with empirical considerations reported in Section 2 and to reproduce or even predict experimental outcomes. In more details, the reported numerical simulations have analyzed the effect on the normal PLL evolution of disruptions in cell proliferation, intercellular adhesion, FGF10 signaling, and SDF1a-driven dynamics. We have also dealt with coupled system perturbations, an aspect not already addressed in the empirical literature, at least to our knowledge.

It is however worth to notice that some refinements are necessary to improve the realism and the potential of the proposed model. First, it has been observed that FGF10-signaling pathways also regulate cell differentiation, which is at the basis of proto-neuromast assembly. However, as far as we know, this process is actually poorly understood. A deeper empirical investigation of the mechanisms defining the exact timing and pattern of PM activation would be fundamental as well.

Another aspect that requires more attention is the influence of the surrounding environment, i.e., it would useful to investigate if the embryonic development of nearby organs and tissues affects, or even regulates, PLL formation. Finally, the identification of a functional relation between the numerically estimated parameters and some measurable quantities would largely improve the predictive potential of the proposed model.

Appendices

A. Parameter estimate

This section will be first devoted to a detailed description of how the model coefficients, listed in Tables 1, have been estimated. Then, we will focus on variations of selected model coefficients in order to further justify the considered parameter setting.

Cell dimensions, proliferation rate and characteristic times of phenotypic transitions. Each cell, regardless of its type, has been set to have a mean diameter d_{c} equal to 7 μm, with a 6 μm-large perinuclear region d_{dupl}, in agreement with the measurements reported in [17]. The common maximal extension of membrane protrusions has been then fixed to $d_{\mathrm{a}} = 20$ μm, consistently with [6, 11] and references therein. The cell proliferation rate γ_{cell} has been set to 4 mitoses/h [17], so that $\Delta t^{\mathrm{dupl}} = 15$ min.

The characteristic times of cell phenotypic changes have been evaluated taking advantage of experimental videos relative to the physiological development of the zebrafish primordium [22, 24]. In particular, the activation of the first progenitor PM cell (located at a distance $l^{\mathrm{PM}\to\mathrm{aPM}} = 16.5$ μm from the rostral edge of the cluster) has been set to occur at $t_1 = 19.1$ hpf. Further PM activations have been then assumed to take place after a delay of $\Delta t^{\mathrm{PM}\to\mathrm{aPM}}$, which has been here hypothesized to be described by a stochastic variable normally distributed, with mean equal to 3.07 h and variance equal to 1.44 h. Also the time-lapses $\Delta t^{\mathrm{dPM}\to\mathrm{pE}}$ and $\Delta t^{\mathrm{pE}\to\mathrm{E}}$, regulating the epithelialization of the cells composing the body of the rosettes, have been set to follow a Gaussian law, the former with mean equal to 4.2 h and variance equal to 1.12 h, the latter with mean equal to 4 h and variance to 1.17 h.

Parameters relative to chemical kinetics. The model parameters characterizing FGF10 and SDF1a kinetics have been mainly estimated according to the experimental literature. In particular, in Eq. (20), the diffusion coefficient of FGF10, D_φ, has been set equal to 10 $\mu\mathrm{m}^2\mathrm{s}^{-1}$, its possible maximal concentration $\varphi_{\max}$ to 1.5 nM, while its decay rate δ_φ to 0.0025 s^{-1}, as in [21]. The secretion rate of the chemical, γ_φ, has been finally assumed to be 0.0083 $\mathrm{nM\,s}^{-1}$, see [8]. In Eq. (21), the diffusion coefficient of SDF1a, D_σ, has been set equal to 0.333 $\mu\mathrm{m}^2\mathrm{s}^{-1}$, and its maximal possible local amount has been fixed to 0.5 nM, see [21]. The SDF1a decay and secretion rates, δ_σ and γ_σ, have been then assumed to be equal to 0.0033 s^{-1} and 0.0033 $\mathrm{nM\,s}^{-1}$, respectively, with $t_{\mathrm{sdf}} = 20$ hpf, in agreement with the empirical quantification reported in [21].

Parameters relative to cell velocity components. Cell dynamics are characterized by the following set of parameters:

$$\left(v_{\mathrm{rand}}, v_{\mathrm{rep}},\ v_{\mathrm{adh}},\ V_{\mathrm{adh}},\ \chi_{\mathrm{sdf}},\ \chi_{\mathrm{fgf}},\ \alpha_4^{\mathrm{sdf}}, \alpha_7^{\mathrm{sdf}}\right) \in \mathbb{R}_+^6 \times (0,1]^2.$$

First, we have reasonably fixed the random velocity coefficient v_{rand} equal to 0.019 $\mu\mathrm{m\,s}^{-1}$, i.e., equal to the mean speed of the primordium [22].

Further simplifications have been obtained by other empirical observations. For instance, experimental evidence has widely shown that during PLL development the component cells form adhesive junctions while remaining well-spaced, i.e., they do not undergo significant compression. The proposed model, and in particular the intercellular interaction velocity components (and relative parameters), has indeed to assure that the computational individuals maintain a sufficient mutual distance over time without scattering. We have indeed looked for the values of $v_{\mathrm{adh}}, V_{\mathrm{adh}}$, and v_{rep} that resulted in $d_{\mathrm{c}} = 7$ μm $\approx d_{\min} >$

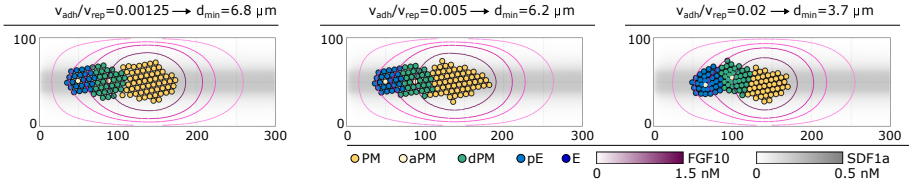

Figure 11: Preliminary simulation run for the estimate of the adhesive/repulsive parameters. Representative configurations taken at $\widetilde{t}$, i.e., at the onset of primordium migration induced by the partial epithelialization of the rosette L1. The initial condition is the same as in the case of the reference setting shown in Fig. 3. However, the cells composing the placode are here subjected only to repulsion, adhesion, differentiation, proliferation and random crawling (i.e., we neglect the chemotactic velocity components). It is possible to see that cell spacing is regulated by the ratio $v_{\rm adh}/v_{\rm rep}$ (or $V_{\rm adh}/v_{\rm rep}$, where $V_{\rm adh} = 2v_{\rm adh}$): if $v_{\rm adh}/v_{\rm rep} \leq 0.005$, realistic configurations where $d_{\rm dupl} < d_{\rm min} \approx d_{\rm c}$ are observed (first and second panels); conversely if $v_{\rm adh}/v_{\rm rep} > 0.005$, cells undergo excessive compression and collapse (third panel), i.e., $d_{\rm min} \ll d_{\rm dupl} < d_{\rm c}$.

$d_{\rm dupl} = 6$ μm, where $d_{\rm min} := \min_{t,i} d_{i,\rm min}(t)$ with $d_{i,\rm min}$ defined in Eq. (5). In this perspective, we have run a series of preliminary simulations where the primordium had the same initial configuration as in the reference case (shown in Fig. 3)) but was only subjected to adhesion, repulsion, proliferation, differentiation and random movement. Such computational realization have been stopped at $\widetilde{t}$, i.e., at the onset of placode migration induced by the partial epithelialization of the firstly-formed rosette L1. In particular, we have neglected the chemical-dependent velocity components (by setting $\mathbf{v}^{\rm fgf} = \mathbf{v}^{\rm sdf} = \mathbf{0}$ in Eq. (9)), since their characteristic coefficients have been estimated later on. For the sake of simplicity, we have also assumed that $V_{\rm adh} = 2v_{\rm adh}$: in the absence of specific empirical measurements, we have hypothesized a two-fold increment in the adhesiveness due to the corresponding state transitions (as done, for instance, in [21]). Cell spacing has been observed to be established by the ratio $v_{\rm adh}/v_{\rm rep}$, rather than by the specific values of $v_{\rm rep}$ and $v_{\rm adh}$, see Fig. 11. In particular, the conditions on the interparticle distance have been shown to be satisfied if $v_{\rm adh}/v_{\rm rep} \leq 0.005$ (i.e., if $V_{\rm adh}/v_{\rm rep} \leq 0.01$): in this respect, we have arbitrarily fixed $v_{\rm adh}/v_{\rm rep} = 0.005$ (i.e., $V_{\rm adh}/v_{\rm rep} = 0.01$).

Experimental assays have then demonstrated that the affinity between SDF1a and *Cxcr7* is nearly ten times higher than the affinity between SDF1a itself and *Cxcr4* [9]. Therefore, in Eq. (17), we have fixed $\alpha_7^{\rm sdf} = 10\alpha_4^{\rm sdf}$. In particular, having assumed that $\alpha_4^{\rm sdf}, \alpha_7^{\rm sdf} \in (0, 1]$, we have established that $\alpha_4^{\rm sdf}$ falls within the range $(0, 0.1]$.

Summing up, all these considerations have allowed us to reduce the set of free parameters to

$$\left(v_{\rm rep} \text{ (or } v_{\rm adh}),\ \chi_{\rm sdf},\ \chi_{\rm fgf},\ \alpha_4^{\rm sdf}(\text{or } \alpha_7^{\rm sdf})\right) \in \mathbb{R}^3_+ \times (0, 0.1] \text{ (or } \times (0, 1]). \quad (24)$$

In the absence of further proper biological considerations or available experimental data, we have finally opted for a simultaneous estimate of the remaining coefficients. In this respect, we have run the complete model (i.e., the so-called reference simulation) and varied the parameters listed in Eq. (24) until a remarkable reproduction of the empirically-observed evolution of *wild-type* primordia

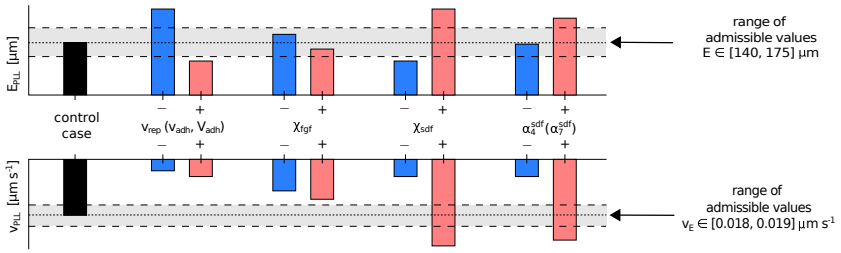

Figure 12: Effect of variation in the reference parameter setting on the critical quantities E_{PLL} (top panel) and v_{PLL} (bottom panel), used to quantify primordium development. In both cases, the grey region denotes the range of admissible values, i.e., $[140, 175]$ μm (top panel) and $[0.018, 0.019]$ $\mu\mathrm{m\,s}^{-1}$ (bottom panel). The control case (black columns) refers to the reference simulation described in Section 5.2. The blue and red columns represent model outcomes obtained by respectively decreasing or increasing one parameter (usually of one order of magnitude or as specified in Section A.1.

has been obtained. In particular, we have selected the values (listed in Table 1) that have allowed to obtain $E_{\mathrm{PLL}} = 158$ μm and $v_{\mathrm{PLL}} = 0.019$ $\mu\mathrm{m\,s}^{-1}$, which fall within the range of their empirically measured counterparts, i.e., $[140, 175]$ μm and $[0.018, 0.019]$ $\mu\mathrm{m\,s}^{-1}$, respectively (see [17, 22, 24]). We finally remark that the chosen parameter setting has also permitted to consistently preserve the plausible intercellular distance $d_{\mathrm{min}} \approx d_{\mathrm{c}}$, which has been firstly obtained in the case of cell dynamics that not accounting for chemotactic contributions.

A.1. Variations in the reference parameter setting

In this section, we analyze the effect on the normal evolution of the computational primordium of variations in the reference parameter setting given, as seen, in Table 1. Such a study also represents a further justification for the employed estimate of the model free coefficients. In particular, in each of the following families of numerical realizations, we decrease/increase the value of one parameter of the group listed in Eq. (24), while maintaining fixed the others (for comparison purposes, the initial condition of the system, the period of observation, the time lapses regulating proto-neuromasts formation and maturation remain unaltered and are set as in the representative reference simulation reported in Fig. 4). The discrepancy of the model outcomes with respect to the reference case in Fig. 4 will be highlighted both qualitatively, i.e., in terms of primordium morphology and migratory behavior, and quantitatively, i.e., in terms of the critical quantities E_{PLL} and v_{PLL} given in Eqs. (22)-(23). In this respect, a summary of the values of E_{PLL} and v_{PLL} resulting from parametric changes is provided in Fig. 12.

Variations of repulsive/adhesive interaction coefficients. We start by varying the intercellular interaction coefficients, however preserving the ratio $v_{\mathrm{adh}}/v_{\mathrm{rep}} = 0.005$ needed to maintain a plausible cell spacing. We also recall that $V_{\mathrm{adh}} = 2v_{\mathrm{adh}}$.

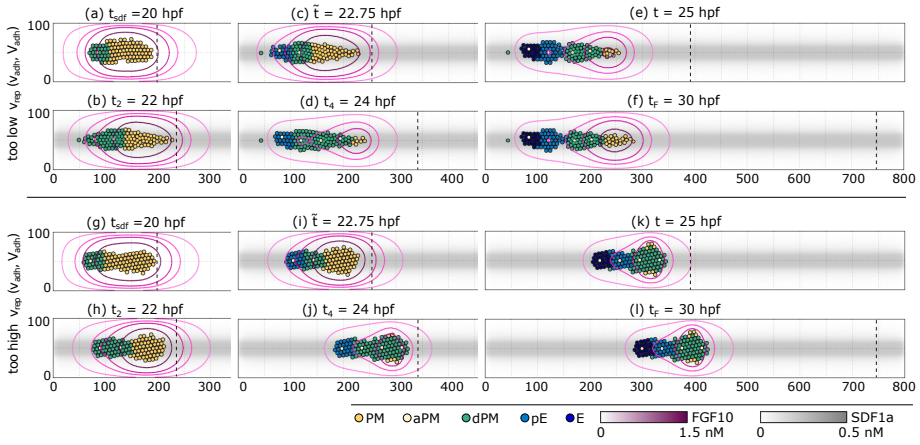

Figure 13: Evolution of the primordium in the case of too low and too high values of the adhesive/repulsive strengths: i.e., $v_{\text{rep}} = 1\ \mu\text{m}\,\text{s}^{-1}$ and $v_{\text{adh}} = 0.005\ \mu\text{m}\,\text{s}^{-1}$ in panels (a)-(f); while $v_{\text{rep}} = 20\ \mu\text{m}\,\text{s}^{-1}$ and $v_{\text{adh}} = 0.1\ \mu\text{m}\,\text{s}^{-1}$ in panels (g)-(l). For visualization purposes, each panel shows only the subregion of the domain that fully contains the primordium. For comparison purposes, at each considered time instant, a dashed black line denotes the position of primordium caudal edge in the reference simulation.

On the one hand, too low values of adhesive/repulsive strengths (for instance obtained by a drop of one order of magnitude, i.e., to $v_{\text{rep}} = 1\ \mu\text{m}\,\text{s}^{-1}$ and $v_{\text{adh}} = 0.005\ \mu\text{m}\,\text{s}^{-1}$) affect the normal evolution of both primordium morphology and migration, see Fig. 12. In fact, an excessive initial elongation of the placode (quantified by $E_{\text{PLL}} = 180\ \mu\text{m}$) is followed by an extremely reduced speed of its migration (as $v_{\text{PLL}} = 0.002\ \mu\text{m}\,\text{s}^{-1}$) and an unrealistical placode fragmentation, see Fig. 13 (a)-(f).

On the other hand, a high enough increment of both interaction parameters (obtained for instance by doubling both coefficients, i.e., by fixing $v_{\text{rep}} = 20\ \mu\text{m}\,\text{s}^{-1}$ and $v_{\text{adh}} = 0.1\ \mu\text{m}\,\text{s}^{-1}$) results in an implausibly compressed and rounded primordium which is not able to normally migrate along the myoseptum (where $E_{\text{PLL}} = 138\ \mu\text{m}$ and $v_{\text{PLL}} = 0.008\ \mu\text{m}\,\text{s}^{-1}$), see Figs. 12 and 13 (g)-(l). In more details, too high interaction parameters substantially increase the intensity of the corresponding velocities, which overcome both SDF1a and FGF10-related dynamics. This, in turn, enhances the placode compactness: the resulting higher cell density finally impedes the normal proliferation of PM individuals as well the formation of the fifth rosette, see Fig. 13 (j)-(l). The over-adhesive intercellular stimuli do not allow the deposition of the mature proto-neuromast as well, which rather remains anchored to the rest of the aggregate and further slows down the entire placode, see Fig. 13 (k)-(l).

Variations of chemical sensitivity parameters. We now vary the cell chemical sensitivity parameters, χ_{fgf} and χ_{sdf}. We recall that the former quantity refers to the level of activity of the FGF10 receptor *fgfr1*, expressed by dPM, pE, and E individuals; the latter is instead relative to the SDF1a migratory related

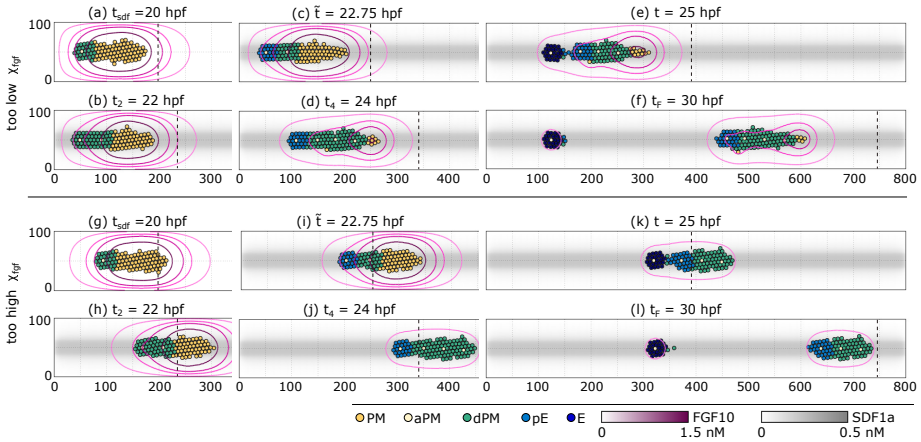

Figure 14: Evolution of the primordium in the case of too low and too high levels of activity of FGF10 receptor *fgfr1*, i.e., $\chi_{\text{fgf}} = 0.01\ \mu\text{m}^2\,\text{s}^{-1}$ in panels (a)-(f); and $\chi_{\text{fgf}} = 0.2\ \mu\text{m}^2\,\text{s}^{-1}$ in panels (g)-(l). For visualization purposes, each panel shows only the subregion of the domain that fully contains the primordium. For comparison purposes, at each considered time instant, a dashed black line denotes the position of primordium caudal edge in the reference simulation.

receptor *Cxcr4*, present in PM, aPM, and dPM particles.

Entering in more details, too low values of χ_{fgf} result in a normal initial stretch of the primordium morphology, followed by a substantially low directional speed: for instance, a drop of one order of magnitude, i.e., down to $\chi_{\text{fgf}} = 0.01\ \mu\text{m}^2\,\text{s}^{-1}$, leads to $E_{\text{PLL}} = 160\ \mu\text{m}\,\text{s}^{-1}$ and $v_{\text{PLL}} = 0.014\ \mu\text{m}\,\text{s}^{-1}$, see Figs. 12 and 14 (a)-(f).

Also too high values of χ_{fgf} do not affect initial placode elongation (e.g., $\chi_{\text{fgf}} = 0.2\ \mu\text{m}^2\,\text{s}^{-1}$ leads to $E_{\text{PLL}} = 156\ \mu\text{m}$). However, they impact on its migratory determinants, see Figs. 12 and 14 (g)-(l). Cell over-sensitivity to FGF10 in fact results in a high intensity of the corresponding velocity component which overcomes the other contributions. Consequently, dPM individuals forming rosettes body are significantly attracted by and push forward with an enhanced force FGF10-producing PM cells located at the caudal region of the aggregate. This mechanism enhances both the initial primordium speed and the compactness of the aggregate w.r.t. the reference simulation, see Fig. 14 (g)-(i). Such a latter consequence in turn causes the disruption of normal proliferation processes which results in a lack of PM agents after the formation of the fourth rosette and therefore in a slowing down of primordium migration (leading to an overall mean speed of $v_{\text{PLL}} = 0.015\ \mu\text{m}\,\text{s}^{-1}$), see Fig. 14 (i)-(l).

Too low values of χ_{sdf} instead determine a substantial decrement in the intensity of the corresponding chemotactic stimulus, which is overcome by the other velocity terms. This results in a more compressed and round primordium morphology (e.g., a drop of one order of magnitude of χ_{sdf}, i.e., down to $0.01\ \mu\text{m}^2\,\text{s}^{-1}$, leads to $E_{\text{PLL}} = 138\ \mu\text{m}$) that, in turn, causes abnormal cell proliferation, eventually, preventing the formation of the fifth rosette, see Figs. 12 and 15 (a)-(f). We observe a substantial drop in the directional speed of the

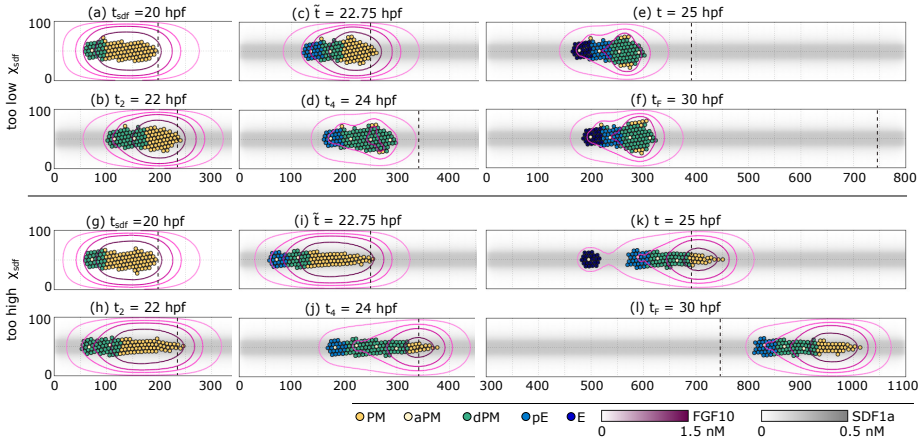

Figure 15: Evolution of the primordium in the case of too low and too high levels of activity of migratory related SDF1a receptor *Cxcr4*, i.e., $\chi_{\rm sdf} = 0.01\ \mu{\rm m}^2\,{\rm s}^{-1}$ in panels (a)-(d) and $\chi_{\rm sdf} = 2\ \mu{\rm m}^2\,{\rm s}^{-1}$ in panels (e)-(h). For visualization purposes, each panel shows only the subregion of the domain that fully contains the primordium. For comparison purposes, at each considered time instant, a dashed black line denotes the position of primordium caudal edge in the reference simulation.

embryonic organ as well, as quantified by $v_{\rm PLL} = 0.003\ \mu{\rm m\,s}^{-1}$ and shown in Figs. 12 and 15 (d)-(f).

Conversely, as shown in Fig. 15 (g)-(k) and summarized in Fig. 12, too high values of $\chi_{\rm sdf}$ first result in an excessive initial elongation of the primordium (for instance $\chi_{\rm sdf} = 0.2\ \mu{\rm m}^2\,{\rm s}^{-1}$ leads to $E_{\rm PLL} = 201\ \mu{\rm m}$), and then in an abnormally fast migration of the aggregate (as quantified by $v_{\rm PLL} = 0.02\ \mu{\rm m}^2\,{\rm s}^{-1}$). The high intensity of SDF1a-related velocity component in fact overcomes the other contributions so that *Cxcr4*-expressing cells are more free to move along the stripe of the chemical.

Variations of the affinity between SDF1a and its receptors. We finally test variations in the affinity of both SDF1a receptors *Cxcr4* and *Cxcr7* for their ligand, i.e., of $\alpha_4^{\rm sdf}, \alpha_7^{\rm sdf} \in (0, 1]$. In this respect, we recall that *Cxcr7* has been experimentally estimated to have an affinity ten times higher than *Cxcr4*, which implies $\alpha_7^{\rm sdf} = 10\alpha_4^{\rm sdf}$ in terms of modeling coefficients, with $\alpha_4^{\rm sdf} \in (0, 0.1]$.

On one hand, as shown in Fig. 12, a drop of both parameters does not significantly affect primordium morphology but causes a substantial slow down of its migration (e.g., by setting $\alpha_4^{\rm sdf} = 0.01$ and $\alpha_7^{\rm sdf} = 0.1$ we obtain to $E_{\rm PLL} = 146\ \mu{\rm m}$ and $v_{\rm PLL} = 0.003\ \mu{\rm m\,s}^{-1}$), see also Fig. 16 (a)-(f). In this respect, it is useful to notice that an almost negligible affinity of both receptors *Cxcr7*/*Cxcr4* to SDF1a does not result in the absence of the SDF1a-driven chemotactic migration (as obtained for instance by full or partial inhibition of the activity of receptor *Cxcr4*, i.e., by decrements in $\chi_{\rm sdf}$). It rather implies that the corresponding velocity component only depends on the distribution of the chemical and not on the cell distribution, because the amount of ligand se-

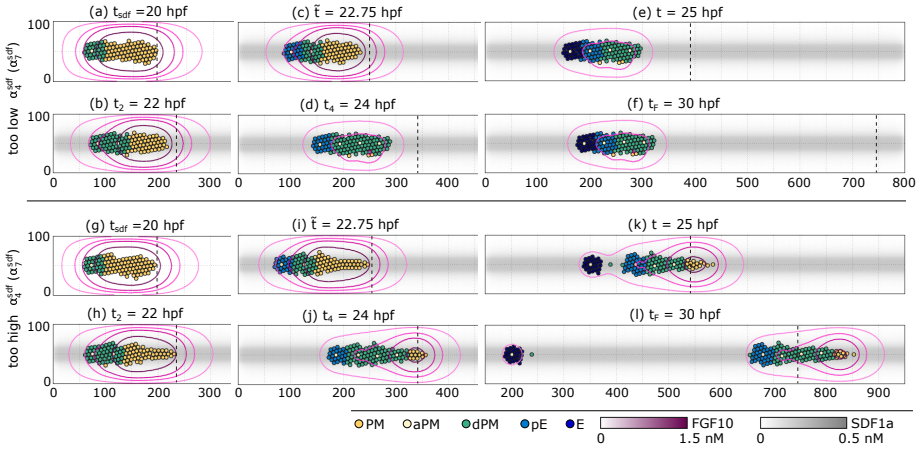

Figure 16: Evolution of the primordium in the case of too low and too high affinity of both SDF1a receptors *Cxcr4* and *Cxcr7* for their ligand, i.e., $\alpha_4^{\mathrm{sdf}} = 0.01$ and $\alpha_7^{\mathrm{sdf}} = 0.1$ in panels (a)-(d); and $\alpha_4^{\mathrm{sdf}} = 0.09$ and $\alpha_7^{\mathrm{sdf}} = 0.9$ in panels (e)-(h). For visualization purposes, each panel shows only the subregion of the domain that fully contains the primordium. For comparison purposes, at each considered time instant, a dashed black line denotes the position of primordium caudal edge in the reference simulation.

questered is almost negligible. Referring to Eqs. (16) and (17), in mathematical terms we have in fact that $W_i^{\mathrm{sdf}} \approx 1$ for any i. Accordingly, the movement of all *Cxcr4*-expressing individuals is substantially aligned towards the central region of the domain $\mathcal{H}$ (i.e., towards the source of the exogenous chemical).

On the other hand, as reported in Fig. 12, too large values of the affinity of both receptors *Cxcr4* and *Cxcr7* for the exogenous chemical enhance both the initial stretching of the primordium and its mean directional speed (e.g., $\alpha_4^{\mathrm{sdf}} = 0.09$ and $\alpha_7^{\mathrm{sdf}} = 0.9$ leads to $E_{\mathrm{PLL}} = 194$ μm and $v_{\mathrm{PLL}} = 0.02$ $\mu\mathrm{m\,s}^{-1}$), see also Fig. 16 (g)-(l). This is probably due to the fact that *Cxcr4*-expressing cells perceive a steeper chemical gradient (and therefore experience an increased chemotactic stimulus) since surrounding individuals are able to sequester a higher fraction of the diffusive molecular substance.

Author Contributions. All authors contributed to conception and design of the study. AC and MS implemented and parameterized the model and conducted the *in silico* simulations. All authors contributed to drafting the manuscript and gave final approval for publication.

Acknowledgments. We acknowledge that the present research has been partially supported by MIUR grant "Dipartimenti di Eccellenza 2018-2022" (Project no. E11G18000350001). AC has been also supported by a Research Grant from the Istituto Nazionale di Alta Matematica "F. Severi" (INdAM).

References

[1] Allena, R., Maini, P., 2014. Reaction-diffusion finite element model of lateral line primordium migration to explore cell leadership. Bulletin of Mathematical Biology 76, 3028 – 3050. doi:10.1007/s11538-014-0043-7.

[2] Aman, A., Nguyen, M., Piotrows, T., 2011. Wnt/β-catenin dependent cell proliferation underlies segmented lateral line morphogenesis. Developmental Cell 349, 470 – 482. doi:10.1016/j.ydbio.2010.10.022.

[3] Aman, A., Piotrowski, T., 2008. Wnt/β-catenin and fgf signaling control collective cell migration by restricting chemokine receptor expression. Developmental Cell 15, 749 – 761. doi:10.1016/j.devcel.2008.10.002.

[4] Cañizo, J., Carrillo, J.A., Patacchini, F.S., 2015. Existence of compactly supported global minimisers for the interaction energy. Archive for Rational Mechanics and Analysis 217, 1197 – 1217. doi:10.1007/s00205-015-0852-3.

[5] Cañizo, J., Patacchini, F.S., 2018. Discrete minimisers are close to continuum minimisers for the interaction energy. Calculus of Variations and Partial Differential Equations 57, 1 – 35. doi:10.1007/s00526-017-1289-3.

[6] Carrillo, J.A., Colombi, A., Scianna, M., 2018. Adhesion and volume constraints via nonlocal interactions determine cell organisation and migration profiles. Journal of Theoretical Biology 445, 75 – 91. doi:10.1016/j.jtbi.2018.02.022.

[7] Chitnis, A., Dalle Nogare, D., 2011. A computational model reveals the remarkable patterning potential of the wnt-fgf gene regulatory network in the posterior latelal line primordium. Developmental Biology 356, 111. doi:10.1016/j.ydbio.2011.05.039.

[8] Dalle Nogare, D., Somers, K., Rao, S., Matsuda, M., Reichman-Fried, M., Raz, E., Chitnis, A.B., 2014. Leading and trailing cells cooperate in collective migration of the zebrafish posterior lateral line primordium. Development 141, 3188 – 3196. doi:10.1242/dev.106690.

[9] Dambly-Chaudière, C., Cubedo, N., Ghysen, A., 2007. Control of cell migration in the development of the posterior lateral line: antagonistic interactions between the chemokine receptors cxcr4 and cxcr7/rdc1. BMC Developmental Biology 7. doi:10.1186/1471-213X-7-23.

[10] David, N.B., Sapède, D., Saint-Etienne, L., Thisse, C., Thisse, B., Dambly-Chaudière, C., Rosa, F.M., Ghysen, A., 2003. Molecular basis of cell migration in the fish lateral line: role of the chemokine receptor cxcr4 and of its ligand, sdf1. Proceedings of the National Academy of Sciences 99, 16297 – 16302. doi:10.1073/pnas.252339399.

[11] Di Costanzo, E., Natalini, R., Preziosi, L., 2015. A hybrid mathematical model for self-organizing cell migration in the zebrafish lateral line. Journal of Mathematical Biology 71, 171 – 214. doi:10.1007/s00285-014-0812-9.

[12] Donà, E., Barry, J.D., Valentin, G., Quirin, C., Khmelinskii, A., Kunze, A., Durdu, S., Newton, L.R., Fernandez-Minan, A., Huber, W., Knop, M., Gilmour, D., 2013. Directional tissue migration through a self-generated chemokine gradient. Nature 503, 285 – 289. doi:10.1038/nature12635.

[13] Drasdo, D., 2003. On selected individual-based approaches to the dynamics in multicellular systems, in: Alt W., Chaplain M., G.M.L.J. (Ed.), Polymer and Cell Dynamics. Mathematics and Biosciences in Interaction.. Birkhäuser, Basel, pp. 169 – 203. doi:10.1007/978-3-0348-8043-5_15.

[14] Durdu, S., Iskar, M., Revenu, C., Schieber, N., Kunze, A., Bork, P., Schwab, Y., Gilmour, D., 2014. Luminal signalling links cell communication to tissue architecture during organogenesis. Nature 515, 120 – 124. doi:10.1038/nature13852.

[15] Ghysen, A., Dambly-Chaudière, C., 2004. Development of the zebrafish lateral line. Current Opinion in Neurobiology 14, 67 – 73. doi:10.1016/j.conb.2004.01.012.

[16] Ghysen, A., Dambly-Chaudière, C., 2007. The lateral line microcosmos. Genes & Development 21, 2118 – 2130. doi:10.1101/gad.1568407.

[17] Gompel, N., Cubedo, N., Thisse, C., Thisse, B., Dambly-Chaudière, C., Ghysen, A., 2001. Pattern formation in the lateral line of zebrafish. Mechanisms of Development 105, 69 – 77. doi:10.1016/S0925-4773(01)00382-3.

[18] Haas, P., Gilmour, D., 2006. Chemokine signaling mediates self-organizing tissue migration in the zebrafish lateral line. Developmental Cell 10, 673 – 680. doi:10.1016/j.devcel.2006.02.019.

[19] Keller, E.T., Murtha, J.M., 2004. The use of mature zebrafish (danio rerio) as a model for human aging and disease. Comparative Biochemistry and Physiology Part C: Toxicology & Pharmacology 138, 335 – 341. doi:10.1016/j.cca.2004.04.001.

[20] Kimmel, C.B., Ballard, W.W., Kimmel, S.R., Ullmann, B., Schilling, T.F., 1995. Stages of embryonic development of the zebrafish. Developmental Dynamics 203, 253 – 310. doi:10.1002/aja.100203030.

[21] Knutsdottir, H., Zmurchok, C., Bhaskar, D., Palsson, E., Dalle Nogare, D., Chitnis, A.B., Edelstein-Keshet, L., 2017. Polarization and migration in the zebrafish posterior lateral line system. PLOS Computational Biology 13, e1005451. doi:10.1371/journal.pcbi.1005451.

[22] Lecaudey, V., Cakan-Akdogan, G., Norton, W.H.J., Gilmour, D., 2008. Dynamic fgf signaling couples morphogenesis and migration in the zebrafish lateral line primordium. Development 135, 2695 – 2705. doi:10.1242/dev.025981.

[23] Metcalfe, W.K., 1985. Sensory neuron growth cones comigrate with posterior lateral line primordial cells in zebrafish. Journal of Comparative Neurology 238, 218 – 224. doi:10.1002/cne.902380208.

[24] Nechiporuk, A., Raible, D.W., 2008. Fgf-dependent mechanosensory organ patterining in zebrafish. Science 320, 1774 – 1777. doi:10.1126/science.1156547.

[25] Revenu, C., Streichan, S., Donà, E., Lecaudey, V., Hufnagel, L., Gilmour, D., 2014. Quantitative cell polarity imaging defines leader-to-follower transitions during collective migration and the key role of microtubule-dependent adherens junction formation. Development 141, 1282 – 1291. doi:10.1242/dev.101675.

[26] Ruelle, D., 1999. Statistical mechanics: rigorous results. Imperial College Press, London and World Scientific Publishing Co. Pte. Ltd., Singapore. doi:doi.org/10.1142/4090.

[27] Scianna, M., Preziosi, L., 2012. Multiscale developments of the cellular potts model. Multiscale Developments of the Cellular Potts Model 10, 342 – 382. doi:10.1137/100812951.

[28] Stone, L.S., 1937. Further experimental studies of the development of lateral-line sense organs in amphibians observed in living and vital stained preparations. Journal of Comparative Neurology 68, 83 – 115. doi:10.1002/cne.900680105.

[29] Streichan, S.J., Valentin, G., Gilmour, D., Hufnagel, L., 2011. Collective cell migration guided by dynamically maintained gradients. Physical Biology 8, 045004. doi:10.1088/1478-3975/8/4/045004.

[30] Streisinger, G., Walker, C., Dower, N., Knauber, D., Singer, F., 1981. Production of clones of homozygous diploid zebra fish (brachydanio rerio). Nature 291, 293 – 296. doi:10.1038/291293a0.

[31] Valentin, G., Haas, P., Gilmour, D., 2007. The chemokine sdf1a coordinates tissue migration through the spatially restricted activation of *Cxcr7* and *Cxcr4b*. Current Biology 17, 1026 – 1031. doi:10.1016/j.cub.2007.05.020.